

A semi-implicit material point method based on fractional-step method for saturated soil

Shyamini Kularathna¹ | Weijian Liang^{1,2}  | Tianchi Zhao^{1,3} |
Bodhinanda Chandra¹  | Jidong Zhao²  | Kenichi Soga¹

¹ Department of Civil and Environmental Engineering, University of California, Berkeley, California, USA

² Department of Civil and Environmental Engineering, Hong Kong University of Science and Technology, Clear Water Way, Kowloon, Hong Kong SAR

³ Department of Geotechnical Engineering, College of Civil Engineering, Tongji University, Shanghai, China

Correspondence

Weijian Liang, Department of Civil and Environmental Engineering, Hong Kong University of Science and Technology, Clear Water Way, Kowloon, Hong Kong SAR.

Email: wliangab@connect.ust.hk

Funding information

Hong Kong University of Science and Technology - Overseas Research Grant; China Scholarship Council, Grant/Award Number: 201806260197; Exxon Mobil Cooperation; University of California Berkeley - Jane Lewis Fellowship; Research Grants Council of Hong Kong, Grant/Award Number: 16207319

[Correction added on May 21, 2021: Funding information section has been updated to include Research Grants Council of Hong Kong (GRF Project No. 16207319).]

Abstract

In this paper, a new formulation of material point method (MPM) to model coupled soil deformation and pore fluid flow problems is presented within the framework of the theory of porous media. The saturated porous medium is assumed to be consisting of incompressible pore fluid and deformable soil skeleton made up of incompressible solid grains. The main difference of the proposed MPM algorithm is the implicit treatment of pore-water pressure which satisfies its incompressibility internal constraint. The resulting solid-fluid coupled equations are solved by using a splitting algorithm based on the Chorin's projection method. The splitting algorithm helps to mitigate numerical instabilities at the incompressibility limit when equal-order interpolation functions are used. The key strengths of the proposed semi-implicit coupled MPM formulation is its capability to reduce pressure oscillations as well as to increase the time step size, which is independent of the fluid incremental strain level and the soil permeability. The proposed semi-implicit MPM is validated by comparing the numerical results with the analytical solutions of several numerical tests, including 1D and 2D plane-strain consolidation problems. To demonstrate the capability of the proposed method in simulating practical engineering problems involving large deformations, a hydraulic process leading to slope failure is studied, and the numerical result is validated by the monitored data.

KEYWORDS

fractional-step method, incompressible pore fluid, material point method, saturated soil, slope instability

1 | INTRODUCTION

Numerical modeling of the complex and dynamic behaviors of soil plays an important role in geotechnical engineering. While soil is a natural component of many substances, its mechanical behavior is mainly governed by the three-phase system of porous soil skeleton, water, and air. Due to the feasibility and computational efficiency in simulating large-scale geotechnical engineering problems, a continuum approach is widely used to describe the motion of a soil body. Within the continuum framework for the numerical analysis of soil as a porous medium, one may find two common approaches: the Lagrangian approach of Biot's theory (BT) and the theory of porous media (TPM). Based on the macroscopic description,

both approaches will lead to the same type of equations.¹ However, the TPM is formulated using the theories of continuum mechanics while BT is a phenomenological model developed through a series of work.^{2–6}

Mesh-based continuum methods, such as the finite element method (FEM), have been widely developed in the past decades for modeling coupled soil-pore-fluid interaction phenomena. Three major variations can be highlighted in the literature: $\mathbf{u} - p$, $\mathbf{u} - \mathbf{U}$ and $\mathbf{u} - \mathbf{v} - p$ (where \mathbf{u} : solid displacement, \mathbf{v} : fluid velocity, p : pore pressure and \mathbf{U} : fluid displacement).^{7–9} Among them, the first two reduced formulations are widely adopted within the mesh-based methods as they simplify the computational flow, yet they are known to have limitations in modeling rapid motions with high-frequency ranges due to the ill-treated pore fluid phase.

Although the mesh-based methods including FEM are robust, efficient, and accurate for many geotechnical engineering problems, they inevitably require complex re-meshing and mapping algorithms while dealing with large deformation problems. On the other hand, mesh-less particle-based methods are well-known for their capabilities of handling large deformations in the absence of grids, though they often struggle to impose essential boundary conditions as the Kronecker-Delta property is hardly satisfied.¹⁰ Over the past few years, the material point method (MPM) has been shown to be useful in simulating complex mechanics during failure and post-failure of soil such as landslides.^{11–20} The MPM is a particle-based method which solves the governing equations on a background computational grid.^{21–23} In MPM, a deformable continuum body is discretized into a set of material points which can move through the background grid accordingly with the velocity field mapped from grid nodes. The mesh-independent material points can, therefore, successfully handle large deformations of history-dependent materials. A detailed review of various numerical methods for the analysis of large mass movement in geotechnical problems is elaborated by Soga et al.²⁴

The conventional MPM formulation for porous media uses conditionally stable forward Euler (explicit) time integration. This choice is favorable in dynamic analysis of history-dependent materials and it is computationally easy to implement. However, the stability of the explicit MPM formulation is restricted by the time step size controlled not only by the sound wave propagation speed in the porous medium but also by the fluid incompressibility constraint and the soil permeability. In the incompressible limit, it is well known that the displacement and pressure function spaces must satisfy the Ladyzhenskaya-Babuška-Brezzi (LBB) conditions or the Zienkiewicz-Taylor patch test for optimal performance of a numerical method.²⁵ The implicit mixed-order integration scheme is often found to be the most optimum and accurate solution to date,²⁶ though its implementation is often numerically demanding, and hence, alternative methods have emerged. Penalty method, selective and reduced integration method are some examples.^{27,28} Another alternative approach to treat the material incompressibility constraint is the fractional-step method (also termed as the projection or splitting approach), which originated from the pioneering work of Chorin²⁹ in solving the incompressible Navier-Stokes fluid flow problems. A detailed review of the advancement of fractional-step methods is available in the literature.³⁰

The objective of this study is to investigate the performance of a stable time-stepping scheme for MPM modeling of saturated porous media. A semi-implicit coupled MPM algorithm is introduced to circumvent the numerical instabilities exhibited in the limits of pore fluid incompressibility and low soil permeability conditions. The fractional-step method is adopted to avoid performance issues while using equal-order interpolation functions for displacement and pressure fields. Several previous studies have demonstrated the use of the fractional-step method in single-phase incompressible MPM.^{31–33} Extending a similar fractional step technique in the present coupled MPM formulation for saturated porous media is a formative approach. Further by implicitly treating the diffusion term, it is shown that a time step size that is independent of the soil permeability can be chosen. The code proposed in the current work is available under an MIT license in Github¹, within the CB-Geo MPM code.³⁴

This paper is organized as follows. First, the kinematics of porous media and the governing equations within the theoretical framework of TPM are described in Section 2. The semi-implicit MPM formulation based on two different splitting techniques is then presented in Section 3. Section 4 outlines the computational implementation of the proposed MPM extension and Section 5 presents several numerical examples to validate the proposed MPM implementation. Conclusions and outlook are drawn in the last section.

2 | KINEMATICS OF POROUS MEDIA AND GOVERNING EQUATIONS

This section outlines the kinematics of soil as a porous medium and the governing equations. The porous medium is assumed to be fully saturated with an incompressible fluid. The mechanical behavior of the solid skeleton and the pore

¹<https://github.com/cb-geo/mpm>

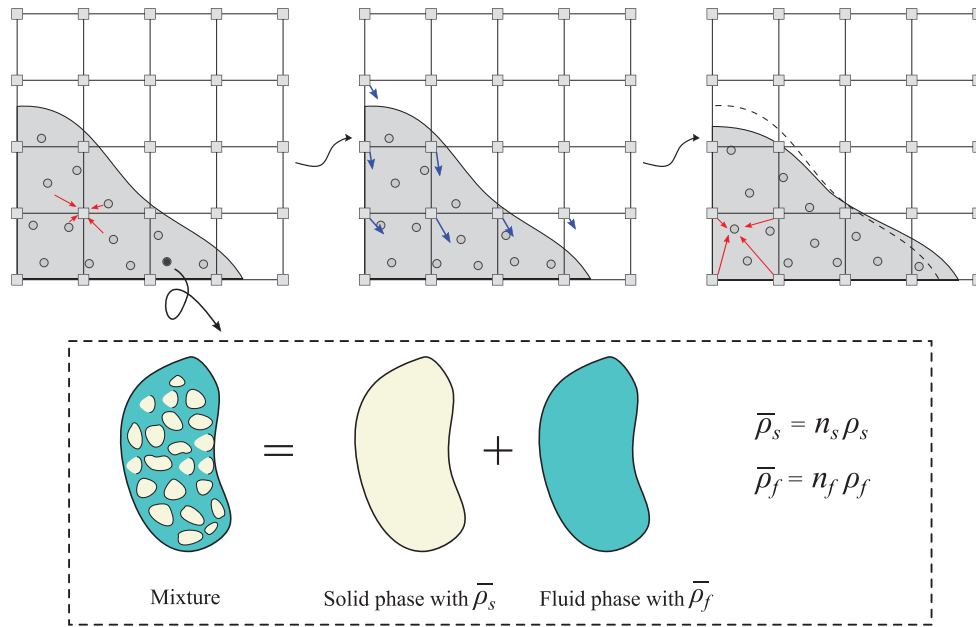


FIGURE 1 A schematic illustration of the single-point-two-phase MPM model. Here, each material point is comprised of solid and liquid phase defined by their respective volume fraction n and effective density $\bar{\rho}$

fluid flow is mathematically described using the concepts of TPM with the following assumptions: (i) iso-thermal condition, (ii) Terzaghi's effective stress principle, (iii) deformable soil skeleton made up of incompressible solid grains, (iv) incompressible pore fluid, (v) pore fluid flow obeys linear Darcy's law, and (vi) the gradient of phase-wise volume fraction is negligible.

2.1 | Preliminaries

In the mathematical derivation described herein, the subscripts s and f denote the soil skeleton and the pore fluid, respectively. The superscript t represents the current time, whereas $t + 1$ is used for advancing to the next time step. Here, Δt is the assumed time increment. The subscript I or J represents the nodes at the background mesh and p is used to identify material points. Note that the hat operator ($\hat{\delta}$) is used to indicate a nodal variable which is particularly useful when expressing the balance equations in a matrix form.

In this study, single-point two-phase MPM framework, which is graphically described in Figure 1, is adopted. Each material point consists of solid-skeleton and pore-fluid phase with volumes V_α ($\alpha = s$ or f) which can be computed from the volume fractions n_α at a given point and time ($V_\alpha = n_\alpha V$, where V is the total mixture volume). The effective density of each phase $\bar{\rho}_\alpha$ is obtained based on $\bar{\rho}_\alpha = n_\alpha \rho_\alpha$ (where ρ_α is the real, intrinsic material density). Here, the deformation of the solid skeleton governs the volume change of the material point.

In the single-point two-phase representation, the motion of the porous medium is controlled by the solid phase. The solid skeleton velocity \mathbf{v}_s and acceleration \mathbf{a}_s defined in a Lagrangian manner carry the material point through the whole computation. For the pore fluid, the kinematic variables include the actual velocity \mathbf{v}_f and acceleration, \mathbf{a}_f . In this manuscript, the intrinsic fluid velocity \mathbf{v}_f is used over the relative (seepage) velocity as it simplifies the application of the Dirichlet boundary condition in the solid-fluid coupled formulation. These motion variables are defined as follows,

$$\mathbf{v}_s = \frac{d_s \mathbf{x}}{dt}, \quad \mathbf{a}_s = \frac{d_s \mathbf{v}_s}{dt}, \quad (1)$$

$$\mathbf{v}_f = \frac{d_f \mathbf{x}}{dt}, \quad \mathbf{a}_f = \frac{d_f \mathbf{v}_f}{dt} = \frac{d_s \mathbf{v}_f}{dt} + (\mathbf{v}_f - \mathbf{v}_s) \cdot \nabla \mathbf{v}_f, \quad (2)$$

where \mathbf{x} is the position vector of material point, and $d_\alpha(\circ)/dt$ indicates the material time derivative with respect to the constituent solid skeleton or pore fluid. This can be expanded as:

$$\frac{d_\alpha(\circ)}{dt} = \frac{\partial(\circ)}{\partial t} + \mathbf{v}_\alpha \cdot \nabla(\circ). \quad (3)$$

The Terzaghi effective stress principle³⁵ is adopted in this study, which states that

$$\boldsymbol{\sigma} = \boldsymbol{\sigma}' - p\mathbf{I}, \quad (4)$$

where $\boldsymbol{\sigma}$ is the total stress, $\boldsymbol{\sigma}'$ is the effective stress, p is the pore water pressure and \mathbf{I} is the identity tensor. In our notation, the stress is assumed to be positive in tension, while the pore water pressure is positive in compression, following the convention in continuum mechanics.

2.2 | Governing equations

2.2.1 | Mass conservation

Assuming there is no mass exchange between constituents, and both solid grains and interstitial pore fluid are incompressible ($d\rho_\alpha/dt = 0$), the mass balance equation for the solid skeleton and pore fluid are expressed as:

$$\frac{d_s n_s}{dt} + n_s \nabla \cdot \mathbf{v}_s = 0, \quad (5)$$

$$\frac{d_f n_f}{dt} + n_f \nabla \cdot \mathbf{v}_f = 0. \quad (6)$$

By adding Equations (5) and (6) and using $n_s + n_f = 1$ for biphasic porous media, the mixture mass balance equation is obtained, which reads as

$$\nabla \cdot (n_s \mathbf{v}_s + n_f \mathbf{v}_f) = 0. \quad (7)$$

Assuming that the phase-wise volume fraction is sufficiently smooth over the entire mixture domain, the volume fraction gradient terms are commonly neglected in the single-point two-phase implementation, and thus, the mass balance Equation (7) can be simplified to:

$$n_s \nabla \cdot \mathbf{v}_s + n_f \nabla \cdot \mathbf{v}_f = 0. \quad (8)$$

As highlighted by Ceccato et al.,³⁶ this hypothesis is reasonable but may induce certain errors when two materials with very different porosity are in contact.

2.2.2 | Momentum conservation

The equations governing the motion of soil as a porous medium are presented in the current subsection. Neglecting the convective term, the linear-momentum balance equations for the solid skeleton and the pore-water phase are:

$$\bar{\rho}_s \mathbf{a}_s = \nabla \cdot (\boldsymbol{\sigma}' - n_s p \mathbf{I}) + \bar{\rho}_s \mathbf{b} - \mathbf{f}_b - \mathbf{f}_d, \quad (9)$$

$$\bar{\rho}_f \mathbf{a}_f = \nabla \cdot (-n_f p \mathbf{I}) + \bar{\rho}_f \mathbf{b} + \mathbf{f}_b + \mathbf{f}_d, \quad (10)$$

where the buoyancy and the viscous drag force, \mathbf{f}_b and \mathbf{f}_d , read

$$\mathbf{f}_b = p \nabla n_f, \quad (11)$$

$$\mathbf{f}_d = -\frac{n_f^2 \rho_f g}{k} (\mathbf{v}_f - \mathbf{v}_s). \quad (12)$$

Here, $g = 9.81 \text{ m/s}^2$ is the earth gravitational acceleration. In the above equations k is the soil mechanics permeability measured in m/s, which may be expressed as a tensor in anisotropic media, and \mathbf{b} is the body force. The linear momentum balance for the mixture is then obtained by summing up Equations (9) and (10) as:

$$\bar{\rho}_s \mathbf{a}_s + \bar{\rho}_f \mathbf{a}_f = \nabla \cdot (\boldsymbol{\sigma}' - p \mathbf{I}) + \rho \mathbf{b}, \quad (13)$$

where $\rho = \bar{\rho}_s + \bar{\rho}_f$ is the density of the mixture. Having Equations (8), (9), (10), and (13) in hand, both the static and dynamic solid-liquid coupled problems can be solved under the full range of acceleration frequencies.³⁷

3 | TIME INTEGRATION AND THE APPLICATION OF FRACTIONAL-STEP METHOD

Although the implementation of the explicit scheme is more straightforward, the explicit formulation is proven to be not feasible for nearly or fully incompressible materials, such as porous materials saturated with pore water, since it is subjected to extremely small time steps to fulfill stability condition. In this study, an extension of the MPM for two-phase material is established based on a semi-implicit scheme,^{38,39} wherein the effective stress is treated explicitly to avoid successive iteration associated with elastoplastic material responses, while the pore-pressure term is treated implicitly by solving the pressure Poisson equation. The temporal discretized governing equations are as follow:

$$\bar{\rho}_s \mathbf{a}_s^{t+1} = \nabla \cdot (\boldsymbol{\sigma}' - n_s p^{t+1} \mathbf{I}) + \bar{\rho}_s \mathbf{b} - \mathbf{f}_d, \quad (14)$$

$$\bar{\rho}_f \mathbf{a}_f^{t+1} = \nabla \cdot (-n_f p^{t+1} \mathbf{I}) + \bar{\rho}_f \mathbf{b} + \mathbf{f}_d, \quad (15)$$

$$n_s \nabla \cdot \mathbf{v}_s^{t+1} + n_f \nabla \cdot \mathbf{v}_f^{t+1} = 0. \quad (16)$$

Although the drag-force term has not been explicitly associated to any time instance in Equations (14) and (15), it is already clear that semi-implicit scheme leads to a strongly coupled set of equations which require simultaneous solutions of acceleration (or velocity) and pressure fields. To solve the solid-fluid coupled system, the fractional-step method, or also known as the splitting scheme, is employed to decouple the computation of pore pressure with the other kinematic variables. Within the fractional-step method, the coupled system is advanced to next step by a prediction-correction substep and only one variable is solved in each substep, that is, originally: $\{\mathbf{v}_\alpha^t, p^t\} \rightarrow \{\mathbf{v}_\alpha^{t+1}, p^{t+1}\}$, whereas the fractional-step method: $\{\mathbf{v}_\alpha^t, p^t\} \rightarrow \{\mathbf{v}_\alpha^*\} \rightarrow \{p^{t+1}\} \rightarrow \{\mathbf{v}_\alpha^{t+1}\}$. Here, the * superscript indicates an intermediate quantity, which will be further explained in the following paragraph. The fractional-step method effectively decouples the entangled variables, making the system solvable in significantly lower computational cost. This scheme also permits basis functions of equal order to approximate the displacement and pressure fields within or near the incompressibility limit.

The fractional-step algorithm used in this study is based on the original Chorin's projection method.²⁹ The computation proceeds by computing an intermediate velocity \mathbf{v}_α^* from an intermediate acceleration field \mathbf{a}_α^* , which does not necessarily satisfy the incompressibility constraint. In our proposed formulation, instead of solving for intermediate and correcting velocities in each time step,^{38,40} the intermediate and correcting accelerations are solved following the convention in MPM. The acceleration term can be split into two parts: intermediate \mathbf{a}_α^* and correcting \mathbf{a}_α^{**} part as:

$$\mathbf{a}_\alpha^{t+1} = \frac{\mathbf{v}_\alpha^{t+1} - \mathbf{v}_\alpha^t}{\Delta t} = \frac{\mathbf{v}_\alpha^{t+1} - \mathbf{v}_\alpha^*}{\Delta t} + \frac{\mathbf{v}_\alpha^* - \mathbf{v}_\alpha^t}{\Delta t} = \mathbf{a}_\alpha^{**} + \mathbf{a}_\alpha^*. \quad (17)$$

TABLE 1 $\mathbf{u} - \mathbf{v} - p$ ($\mathbf{a}_f \neq 0$) type formulation based on the fractional-step method

Index	Balance equations
A1	Mixture momentum balance equation
i	$\bar{\rho}_s \mathbf{a}_s^* + \bar{\rho}_f \mathbf{a}_f^* = \nabla \cdot (\boldsymbol{\sigma}' - \beta p^t \mathbf{I}) + \rho \mathbf{b}$
ii	$\bar{\rho}_s \mathbf{a}_s^{**} + \bar{\rho}_f \mathbf{a}_f^{**} = -\nabla(p^{t+1} - \beta p^t)$
A2	Solid momentum balance equation
i	$\bar{\rho}_s \mathbf{a}_s^* - \Delta t \frac{n_f^2 \rho_f g}{k} (\mathbf{a}_f^* - \mathbf{a}_s^*) = \nabla \cdot (\boldsymbol{\sigma}' - \beta n_s p^t \mathbf{I}) + \bar{\rho}_s \mathbf{b} + \frac{n_f^2 \rho_f g}{k} (\mathbf{v}_f^t - \mathbf{v}_s^t)$
ii	$\bar{\rho}_s \mathbf{a}_s^{**} = -n_s \nabla(p^{t+1} - \beta p^t)$
A3	Water momentum balance equation
i	$\bar{\rho}_f \mathbf{a}_f^* + \Delta t \frac{n_f^2 \rho_f g}{k} (\mathbf{a}_f^* - \mathbf{a}_s^*) = -\beta n_f \nabla p^t + \bar{\rho}_f \mathbf{b} - \frac{n_f^2 \rho_f g}{k} (\mathbf{v}_f^t - \mathbf{v}_s^t)$
ii	$\bar{\rho}_f \mathbf{a}_f^{**} = -n_f \nabla(p^{t+1} - \beta p^t)$
A4	Mixture mass balance equation
	$\Delta t \left(\frac{n_s}{\rho_s} + \frac{n_f}{\rho_f} \right) \nabla^2 (p^{t+1} - \beta p^t) = n_s \nabla \cdot (\mathbf{v}_s^t + \mathbf{a}_s^* \Delta t) + n_f \nabla \cdot (\mathbf{v}_f^t + \mathbf{a}_f^* \Delta t)$

Following this step, the pore pressure is then computed to satisfy the mass conservation equation of the mixture. Here, the pore pressure also acts as the Lagrange multiplier to the internal incompressibility constraint of the fluid phase that is indirectly related to the mixture balance equation. Finally, the intermediate acceleration and velocity fields are corrected by using the updated pressure gradient.

With the aid of intermediate acceleration, the momentum equations, Equations (14) and (15), can be split to separate the pore-pressure field p^{t+1} from the acceleration field \mathbf{a}_α^{t+1} . The split momentum equations in conjugation with the mass conservation equation are shown in Table 1. The mixture mass balance equation (A4) in Table 1 is obtained by taking the divergence of \mathbf{v}_s^* and \mathbf{v}_f^* from the split momentum balance equations and substituting it to Equation (16).

In applying the fractional-step method, a scalar parameters β has been used to generalize different versions of the derivation, wherein $\beta = 1$ represents the incremental fractional step, while $\beta = 0$ denotes the non-incremental fractional-step approach as introduced originally by Chorin.²⁹ A previous study⁴¹ has shown that the non-incremental version of the fractional step scheme exhibits stable results for the single-phase MPM formulation. In this paper, a similar comparison of the accuracy and stability of the two schemes implemented in the two-phase MPM is conducted and discussed.

It is also worth noting that, in Equations (A2)(i) and (A3)(i) of Table 1, the interaction force between the solid skeleton and pore fluid, that is, the drag force, is evaluated implicitly at the intermediate stage based on the intermediate velocity (or acceleration). Here, Equation (12) can be rewritten and expanded as:

$$\mathbf{f}_d = -\frac{n_f^2 \rho_f g}{k} (\mathbf{v}_f^* - \mathbf{v}_s^*) = -\frac{n_f^2 \rho_f g}{k} \left[(\mathbf{v}_f^t - \mathbf{v}_s^t) - \Delta t (\mathbf{a}_f^* - \mathbf{a}_s^*) \right]. \quad (18)$$

Note that, the first term written in Equation (18) is known from the current step of velocity, whereas the second term is unknown and needs to be evaluated. This choice of scheme may lead to a larger time step size which is also independent of the permeability of the porous media (see further discussion in Section 4.5). Similar treatment is previously adopted by Markert et al.³⁸

4 | FRACTIONAL-STEP ALGORITHM FOR HYDRO-MECHANICAL COUPLED MPM

4.1 | Weak form of the governing equations

Following the standard Galerkin procedure, the weak form of the governing equations is obtained by multiplying equations listed in Table 1 by arbitrary test functions, $\delta \mathbf{v}$ and δp (which also satisfy the same geometric boundary conditions), and integrating over the current material domain, Ω . The weak forms of the momentum balance equations are written as follows:

- Splitting momentum equation for mixture (A1) to (i) a predictor:

$$\int_{\Omega} \delta \mathbf{v} \cdot \bar{\rho}_s \mathbf{a}_s^* d\Omega + \int_{\Omega} \delta \mathbf{v} \cdot \bar{\rho}_f \mathbf{a}_f^* d\Omega = \int_{\Omega} \delta \mathbf{v} \nabla \cdot (\boldsymbol{\sigma}' - \beta p^t \mathbf{I}) d\Omega + \int_{\Omega} \delta \mathbf{v} \cdot \rho \mathbf{b} d\Omega, \quad (19)$$

and (ii) a corrector:

$$\int_{\Omega} \delta \mathbf{v} \cdot \bar{\rho}_s(\mathbf{a}_s^{**}) d\Omega + \int_{\Omega} \delta \mathbf{v} \cdot \bar{\rho}_f(\mathbf{a}_f^{**}) d\Omega = - \int_{\Omega} \delta \mathbf{v} \cdot \nabla(p^{t+1} - \beta p^t) d\Omega. \quad (20)$$

- Splitting momentum equation for solid (A2) to (i) a predictor:

$$\begin{aligned} \int_{\Omega} \delta \mathbf{v} \cdot \bar{\rho}_s \mathbf{a}_s^* d\Omega - \int_{\Omega} \delta \mathbf{v} \cdot \Delta t \frac{n_f^2 \rho_f g}{k} (\mathbf{a}_f^* - \mathbf{a}_s^*) d\Omega = \\ - \int_{\Omega} \delta \mathbf{v} \nabla \cdot (\boldsymbol{\sigma}' - \beta n_s p^t \mathbf{I}) d\Omega + \int_{\Omega} \delta \mathbf{v} \cdot \bar{\rho}_s \mathbf{b} d\Omega + \int_{\Omega} \delta \mathbf{v} \cdot \frac{n_f^2 \rho_f g}{k} (\mathbf{v}_s^t - \mathbf{v}_f^t) d\Omega, \end{aligned} \quad (21)$$

and (ii) a corrector:

$$\int_{\Omega} \delta \mathbf{v} \cdot \bar{\rho}_s(\mathbf{a}_s^{**}) d\Omega = - \int_{\Omega} \delta \mathbf{v} \cdot n_s \nabla(p^{t+1} - \beta p^t) d\Omega. \quad (22)$$

- Splitting momentum equation for fluid (A3) to (i) a predictor:

$$\begin{aligned} \int_{\Omega} \delta \mathbf{v} \cdot \bar{\rho}_f \mathbf{a}_f^* d\Omega + \int_{\Omega} \delta \mathbf{v} \cdot \Delta t \frac{n_f^2 \rho_f g}{k} (\mathbf{a}_f^* - \mathbf{a}_s^*) d\Omega = \\ - \int_{\Omega} \delta \mathbf{v} \cdot \beta n_f \nabla p^t d\Omega + \int_{\Omega} \delta \mathbf{v} \cdot \bar{\rho}_f \mathbf{b} d\Omega - \int_{\Omega} \delta \mathbf{v} \cdot \frac{n_f^2 \rho_f g}{k} (\mathbf{v}_s^t - \mathbf{v}_f^t) d\Omega, \end{aligned} \quad (23)$$

and (ii) a corrector:

$$\int_{\Omega} \delta \mathbf{v} \cdot \bar{\rho}_f(\mathbf{a}_f^{**}) d\Omega = - \int_{\Omega} \delta \mathbf{v} \cdot n_f \nabla(p^{t+1} - \beta p^t) d\Omega. \quad (24)$$

On top of the aforementioned momentum balance equations, the weak form of the mixture mass balance equation (A4) can be written as:

$$\Delta t \int_{\Omega} \delta p \left(\frac{n_s}{\rho_s} + \frac{n_f}{\rho_f} \right) \nabla^2(p^{t+1} - \beta p^t) d\Omega = \int_{\Omega} \delta p n_s \nabla \cdot (\mathbf{v}_s^t + \mathbf{a}_s^* \Delta t) d\Omega + \int_{\Omega} \delta p n_f \nabla \cdot (\mathbf{v}_f^t + \mathbf{a}_f^* \Delta t) d\Omega. \quad (25)$$

In the implementation of the proposed fractional-step algorithm in MPM, the momentum equation for the mixture (19) will be used along with Equation (23) to predict the intermediate acceleration and velocity of the two phases. Equation (19) is preferred over the solid momentum predictor Equation (21) as the latter one requires the separation of the applied total external forces into solid and pore water components. By using the overall mixture phase, the regular Neumann traction boundary condition can be applied without any modification as a predictor step. It should be noted, however, after the pore pressure is computed, instead of using Equation (20) to correct the solid acceleration, Equation (22) is preferred as there is no need to couple the correction term for the two phases. By doing so, the corrected acceleration terms can be computed explicitly considering a lumped-mass matrix at each computational node.

4.2 | Spatial discretization

In the MPM, the spatial discretization proceeds similarly to the FEM. In conventional finite element analysis, the basis function for the displacement field is often set to be one order higher than that of the pressure field to fulfill the Ladyzhenskaya-Babuška-Brezzi (LBB) conditions,²⁵ and thus, avoiding instability. However, as the proposed MPM extension is based on the fractional-step method, it permits an equal-order interpolation function for both displacement and pressure. The interpolation of those variables is written as follow:

$$\mathbf{a}_\alpha(\mathbf{x}, t) = \sum_{I=1}^{n_n} N_I(\mathbf{x}, t) \hat{\mathbf{a}}_{\alpha, I}, \quad \mathbf{a}_\alpha^*(\mathbf{x}, t) = \sum_{I=1}^{n_n} N_I(\mathbf{x}, t) \hat{\mathbf{a}}_{\alpha, I}^*, \quad (26)$$

$$\mathbf{v}_\alpha(\mathbf{x}, t) = \sum_{I=1}^{n_n} N_I(\mathbf{x}, t) \hat{\mathbf{v}}_{\alpha, I}, \quad \mathbf{v}_\alpha^*(\mathbf{x}, t) = \sum_{I=1}^{n_n} N_I(\mathbf{x}, t) \hat{\mathbf{v}}_{\alpha, I}^*, \quad (27)$$

$$p(\mathbf{x}, t) = \sum_{I=1}^{n_n} N_I(\mathbf{x}, t) \hat{p}_I, \quad (28)$$

where n_n is the number of computational node per element, and $N_I(\mathbf{x})$ is the assumed basis function. Here, the nodal velocity, acceleration for phase α and pore pressure in node I are denoted as $\hat{\mathbf{v}}_{\alpha, I}$, $\hat{\mathbf{a}}_{\alpha, I}$, and \hat{p}_I , respectively. Similarly, the test functions can also be written in terms of their nodal values using the same basis functions as:

$$\delta \mathbf{v}_\alpha(\mathbf{x}, t) = \sum_{I=1}^{n_n} N_I(\mathbf{x}, t) \delta \hat{\mathbf{v}}_{\alpha, I}, \quad \delta p(\mathbf{x}, t) = \sum_{I=1}^{n_n} N_I(\mathbf{x}, t) \delta \hat{p}_I. \quad (29)$$

Substituting Equations (26)–(29) into the split predictor Equations (19) and (23) and taking out the nodal trial functions from the integral yield the following spatial discretized equations:

$$\begin{aligned} \mathbf{M}_s \hat{\mathbf{a}}_s^* + \mathbf{M}_f \hat{\mathbf{a}}_f^* &= \mathbf{f}^{int} + \mathbf{f}^{ext}, \\ \mathbf{M}_f \hat{\mathbf{a}}_f^* + \Delta t \mathbf{Q} (\hat{\mathbf{a}}_f^* - \hat{\mathbf{a}}_s^*) &= \mathbf{f}_f^{int} + \mathbf{f}_f^{ext} - \mathbf{Q} (\hat{\mathbf{v}}_f^t - \hat{\mathbf{v}}_s^t), \end{aligned} \quad (30)$$

where,

$$\mathbf{M}_\alpha = \sum_{I=1}^{n_n} \sum_{J=1}^{n_n} \int_{\Omega} \bar{\rho}_\alpha(\mathbf{x}, t) N_I(\mathbf{x}, t) N_J(\mathbf{x}, t) d\Omega, \quad (31)$$

$$\mathbf{Q} = \sum_{I=1}^{n_n} \sum_{J=1}^{n_n} \rho_f g \int_{\Omega} \frac{n_f^2(\mathbf{x}, t)}{k(\mathbf{x}, t)} N_I(\mathbf{x}, t) N_J(\mathbf{x}, t) d\Omega, \quad (32)$$

$$\mathbf{f}^{int} = - \sum_{I=1}^{n_n} \int_{\Omega} \nabla N_I(\mathbf{x}, t) : (\boldsymbol{\sigma}' - \beta p^t \mathbf{I}) d\Omega, \quad (33)$$

$$\mathbf{f}^{ext} = \sum_{I=1}^{n_n} \int_{\Omega} \rho(\mathbf{x}, t) N_I(\mathbf{x}, t) \mathbf{b} d\Omega + \sum_{I=1}^{n_n} \int_{\partial\Omega} N_I(\mathbf{x}, t) \mathbf{t} dS, \quad (34)$$

$$\mathbf{f}_f^{int} = - \sum_{I=1}^{n_n} \int_{\Omega} \nabla N_I(\mathbf{x}, t) : (-\beta n_f p^t \mathbf{I}) d\Omega, \quad (35)$$

$$\mathbf{f}_f^{ext} = \sum_{I=1}^{n_n} \int_{\Omega} \bar{\rho}_f(\mathbf{x}, t) N_I(\mathbf{x}, t) \mathbf{b} d\Omega + \sum_{I=1}^{n_n} \int_{\partial\Omega} N_I(\mathbf{x}, t) \mathbf{t}_f dS. \quad (36)$$

Here, the surface traction forces are defined as $\mathbf{t} = (\boldsymbol{\sigma}' - \beta p \mathbf{I}) \cdot \mathbf{n}$ and $\mathbf{t}_f = -\beta n_f p \cdot \mathbf{n}$, where \mathbf{n} is the surface outward unit normal vector.

Next, following the discretization of the predictor equations, the nodal intermediate velocity $\hat{\mathbf{v}}_\alpha^*$ is calculated from the intermediate acceleration term as:

$$\hat{\mathbf{v}}_\alpha^* = \hat{\mathbf{v}}_\alpha^t + \Delta t \hat{\mathbf{a}}_\alpha^*. \quad (37)$$

The integration by parts and the divergence theorem are applied into Equation (25), which results in an elliptic equation for the pore pressure described in its spatially discretized form as:

$$\mathbf{L} (\hat{p}^{t+1} - \beta \hat{p}^t) = \frac{1}{\Delta t} (\bar{\mathbf{f}} + \bar{\mathbf{f}}_\nu), \quad (38)$$

where,

$$\mathbf{L} = \sum_{I=1}^{n_n} \sum_{J=1}^{n_n} \int_{\Omega} \left[\frac{n_s(\mathbf{x}, t)}{\rho_s} + \frac{n_f(\mathbf{x}, t)}{\rho_f} \right] \nabla N_I(\mathbf{x}, t) \nabla N_J(\mathbf{x}, t) d\Omega, \quad (39)$$

$$\bar{\mathbf{f}} = - \left[\sum_{I=1}^{n_n} \sum_{J=1}^{n_n} \int_{\Omega} \nabla N_I(\mathbf{x}, t) N_J(\mathbf{x}, t) d\Omega \right] \hat{\mathbf{v}}_s^* + \left[\sum_{I=1}^{n_n} \sum_{J=1}^{n_n} \int_{\Omega} \nabla N_I(\mathbf{x}, t) N_J(\mathbf{x}, t) n_f(\mathbf{x}, t) d\Omega \right] (\hat{\mathbf{v}}_f^* - \hat{\mathbf{v}}_s^*), \quad (40)$$

$$\bar{\mathbf{f}}_\nu = \sum_{I=1}^{n_n} \int_{\partial\Omega} N_I(\mathbf{x}, t) \left[-n_f (\hat{\mathbf{v}}_f^* - \hat{\mathbf{v}}_s^*) + \Delta t \left(\frac{n_s}{\rho_s} + \frac{n_f}{\rho_f} \right) \nabla (p^{t+1} - \beta p^t) \right] \cdot \mathbf{n} dS. \quad (41)$$

After solving the pressure Poisson equation, the corrected nodal acceleration can be computed by applying the pressure gradient computed from Equation (38) into Equations (22) and (24) as expressed in the following algebraic equations:

$$\begin{aligned} \mathbf{M}_s \hat{\mathbf{a}}_s^{**} &= \mathbf{G}_s (\hat{p}^{t+1} - \beta \hat{p}^t), \\ \mathbf{M}_f \hat{\mathbf{a}}_f^{**} &= \mathbf{G}_f (\hat{p}^{t+1} - \beta \hat{p}^t), \end{aligned} \quad (42)$$

where \mathbf{M}_α is defined at Equation (31) and \mathbf{G}_α is defined as follows for the two phases:

$$\mathbf{G}_\alpha = - \sum_{I=1}^{n_n} \sum_{J=1}^{n_n} \int_{\Omega} n_\alpha(\mathbf{x}, t) N_I(\mathbf{x}, t) \nabla N_J(\mathbf{x}, t) d\Omega. \quad (43)$$

Having the correcting acceleration terms in hand, the next-step nodal solid- and fluid-phase velocities and accelerations can be obtained simply by:

$$\hat{\mathbf{a}}_\alpha^{t+1} = \hat{\mathbf{a}}_\alpha^* + \hat{\mathbf{a}}_\alpha^{**}, \quad (44)$$

$$\hat{\mathbf{v}}_\alpha^{t+1} = \hat{\mathbf{v}}_\alpha^* + \Delta t \hat{\mathbf{a}}_\alpha^{**}. \quad (45)$$

4.3 | Material point discretization and computation procedure

In the MPM, the geometry of body B in the initial configuration can be approximated and subdivided into n_p material points as:

$$B \approx \sum_{p=1}^{n_p} \Omega_p, \quad (46)$$

Algorithm 1 Fractional-step one-point two-phase MPM algorithm

```

1 if  $t = 0$  then
2   # Initialize material points ;
3   volume:  $V_p^0$ , density:  $\rho_{\alpha,p}^0$ , volume fraction:  $n_{\alpha,p}^0$ , particle mass:  $m_{\alpha,p}^0 = n_{\alpha,p}^0 \rho_{\alpha,p}^0 V_p^0$  ;
4   particle initial total stress:  $\sigma_p^0$ , pore pressure,  $p_p^0$ , particle velocities:  $\mathbf{v}_{s,p}^0$  and  $\mathbf{v}_{f,p}^0$  ;
5 while  $0 < t$  and  $t \leq t_{end}$  do
6   Map particle mass and momentum to computational nodes, and compute nodal velocities – (48), (49) ;
7   Compute solid strain and effective stress – (50)-(53) ;
8   Update particle volume, density, volume fraction, and permeability – (55)-(58) ;
9   Solve for intermediate accelerations,  $\hat{\mathbf{a}}_s^*$  and  $\hat{\mathbf{a}}_f^*$  – (59)-(65);
10  Update intermediate velocities,  $\hat{\mathbf{v}}_s^*$  and  $\hat{\mathbf{v}}_f^*$  – (37) ;
11  Solve the pressure Poisson equation for incremental pressure field,  $(\hat{p}^{t+1} - \beta \hat{p}^t)$  – (66)-(69) ;
12  Solve for correcting accelerations,  $\hat{\mathbf{a}}_s^{**}$  and  $\hat{\mathbf{a}}_f^{**}$  – (70), (71) ;
13  Update nodal accelerations and velocities,  $\hat{\mathbf{v}}_\alpha^{t+1}$  and  $\hat{\mathbf{a}}_\alpha^{t+1}$  – (44), (45) ;
14  Update particle velocity, acceleration, and pressure – (72)-(75) ;
15   $t = t + \Delta t$ 

```

where Ω_p denotes the material volume of each material point. The continuous volume integral found in the weak formulations then can be approximated as:

$$\int_{\Omega} (\dots) d\Omega \approx \sum_{p=1}^{n_p} \int_{\Omega_p} (\dots) d\Omega_p = \sum_{p=1}^{n_p} (\dots) V_p, \quad (47)$$

where the last term can be written assuming that all the quantities inside the volume integral are independent of the volume.

The semi-implicit MPM formulation listed in Table 1 solves for the following three primary variables: (i) acceleration of the solid skeleton \mathbf{a}_s^{t+1} , (ii) acceleration of pore fluid \mathbf{a}_f^{t+1} , and (iii) pore pressure p^{t+1} . Since the fractional-step algorithm is employed, two new variables are introduced: the intermediate acceleration \mathbf{a}_s^* of the solid skeleton and \mathbf{a}_f^* for the pore water phase. In this context, five equations are required to solve the problem at a given time t in addition to the constitutive equation for the solid phase to close the kinematic and equilibrium system. The computation procedure for the proposed fractional-step method based MPM is summarized in Algorithm 1, whereas the explicit MPM scheme is provided for comparison by Algorithm 2 listed in Appendix A.

4.3.1 | Mapping of variables from particles to nodes

At the beginning of each time step, the mass and the velocities of each constituent carried by the material points are mapped to the background grid by the following expressions:

$$\hat{m}_{\alpha,I} = \sum_{p=1}^{n_p} N_I(\mathbf{x}_p^t) m_{\alpha,p}, \quad (48)$$

$$\hat{\mathbf{v}}_{\alpha,I}^t = \frac{\sum_{p=1}^{n_p} N_I(\mathbf{x}_p^t) m_{\alpha,p} \mathbf{v}_{\alpha,p}^t}{\hat{m}_{\alpha,I}}, \quad (49)$$

where n_p is the number of material points associated with node I , and $N_I(\mathbf{x}_p^t)$ is the nodal basis function evaluated at the position of a material point p .

4.3.2 | Effective stress calculation

Assuming the updated stress first (USF) scheme,⁴² the strain and the effective stress of the solid skeleton can be computed incrementally at material point p in the case of small deformation as:

$$\Delta \boldsymbol{\varepsilon}_{s,p}^t = \frac{1}{2} \Delta t \sum_{I=1}^{n_n} \left(\nabla N_I(\mathbf{x}_p^t) \hat{\mathbf{v}}_{s,I}^t + \left(\nabla N_I(\mathbf{x}_p^t) \hat{\mathbf{v}}_{s,I}^t \right)^T \right), \quad (50)$$

$$\Delta \boldsymbol{\sigma}'_p = \mathbb{D} \Delta \boldsymbol{\varepsilon}_{s,p}^t, \quad (51)$$

$$\boldsymbol{\sigma}'_p{}^{t+1} = \boldsymbol{\sigma}'_p{}^t + \Delta \boldsymbol{\sigma}'_p, \quad (52)$$

where \mathbb{D} is the elastoplastic tangent modulus. In the current work, linear elastic and conventional elastoplastic models are used, though the proposed formulation should work for any constitutive models. As the focus of this study is placed upon the fractional-step algorithm, the implementation of the constitutive model will not be repeated here. Readers can refer to our prior work⁴³ for a detailed discussion of the constitutive model implementation in MPM.

In the case of finite deformation with severe rotation, the stress increment $\Delta \boldsymbol{\sigma}'_p$ does not represent the objective stress rate adequately. Therefore, a more appropriate stress update, for example, the Jaumann rate, can be used to update the effective stress:

$$\boldsymbol{\sigma}'_p{}^{t+1} = \boldsymbol{\sigma}'_p{}^t + \Delta \boldsymbol{\sigma}'_p + \Delta t (\boldsymbol{\sigma}'_p{}^t \cdot \mathbf{W}_p^t - \mathbf{W}_p^t \cdot \boldsymbol{\sigma}'_p{}^t), \quad (53)$$

where \mathbf{W}_p^t is the vorticity tensor computed as:

$$\mathbf{W}_p^t = \frac{1}{2} \sum_{I=1}^{n_n} \left(\nabla N_I(\mathbf{x}_p^t) \hat{\mathbf{v}}_{s,I}^t - \left(\nabla N_I(\mathbf{x}_p^t) \hat{\mathbf{v}}_{s,I}^t \right)^T \right). \quad (54)$$

4.3.3 | Computing particle volume, porosity, and permeability

Accordingly, the volume of material points, which represents the mixture, can be updated using the strain increment of the solid skeleton assuming a small deformation theory,

$$V_p^{t+1} = V_p^t \left(1 + \Delta \boldsymbol{\varepsilon}_{vol,p}^t \right), \quad (55)$$

where $\Delta \boldsymbol{\varepsilon}_{vol,p}$ is the incremental volumetric strain, which can be obtained generally by $\Delta \boldsymbol{\varepsilon}_{vol,p} = \det(\Delta \mathbf{F}_p) - 1$ for large deformation assumptions, or by simply performing a trace operation over the strain tensor, that is, $\Delta \boldsymbol{\varepsilon}_{vol,p} = \text{tr}(\Delta \boldsymbol{\varepsilon}_{s,p})$, in small deformation assumptions. In the expression above, $\Delta \mathbf{F}_p = \mathbf{I} + \Delta t \sum_{I=1}^{n_n} \nabla N_I(\mathbf{x}_p^t) \hat{\mathbf{v}}_{s,I}^t$ denotes the increment of deformation gradient at the particle. Furthermore, the density of the mixture and the liquid volume fraction can be updated as follows:

$$\rho_p^{t+1} = \frac{\rho_p^t}{\left(1 + \Delta \boldsymbol{\varepsilon}_{vol,p}^t \right)}, \quad (56)$$

$$n_f^{t+1} = 1 - \frac{1 - n_f^t}{\left(1 + \Delta \boldsymbol{\varepsilon}_{vol,p}^t \right)}. \quad (57)$$

Here, the solid volume fraction n_s can be updated simply by subtraction as $n_s^{t+1} = 1 - n_f^{t+1}$.

Following the update of liquid volume fraction, the coefficient of soil permeability k can be computed. Here, the Kozeny-Carman equation⁴⁴ is used to update the soil permeability, which can be expressed as:

$$k^{t+1} = C \frac{\left(n_f^{t+1} \right)^3}{\left(1 - n_f^{t+1} \right)^2}, \quad (58)$$

where the coefficient C is a parameter that can be determined experimentally considering grain size distribution, grain shape, and the roughness of grains. Together with the permeability and the liquid unit weight, the drag force, Equation (18), can be approximated from the intermediate relative velocity between liquid and solid phase.

4.3.4 | Fractional-step prediction

Having the effective stress and necessary parameters in hand, the following step solves the coupled algebraic equation, Equation (30), which gives the solution for $\hat{\mathbf{a}}_s^*$ and $\hat{\mathbf{a}}_f^*$ for each computational node. Equation (30) can be written in its matrix form element-wise as:

$$\begin{bmatrix} \mathbf{M}_s & \mathbf{M}_f \\ -\Delta t \mathbf{Q} & \mathbf{M}_f + \Delta t \mathbf{Q} \end{bmatrix} \begin{bmatrix} \hat{\mathbf{a}}_s^* \\ \hat{\mathbf{a}}_f^* \end{bmatrix} = \begin{bmatrix} \mathbf{f}^{int} + \mathbf{f}^{ext} \\ \mathbf{f}_f^{int} + \mathbf{f}_f^{ext} - \mathbf{Q}(\hat{\mathbf{v}}_f^t - \hat{\mathbf{v}}_s^t) \end{bmatrix}, \quad (59)$$

where the components constructing the linear systems can be obtained by integrating Equations (31) - (36) via material points' volume as noted previously in Equation (47). One can rewrite those equations as:

$$\mathbf{M}_\alpha = \sum_{p=1}^{n_p} \sum_{I=1}^{n_n} \sum_{J=1}^{n_n} \bar{\rho}_{\alpha,p}^{t+1} N_I(\mathbf{x}_p^t) N_J(\mathbf{x}_p^t) V_p^{t+1}, \quad (60)$$

$$\mathbf{Q} = \sum_{p=1}^{n_p} \sum_{I=1}^{n_n} \sum_{J=1}^{n_n} \rho_f g \frac{(n_{f,p}^{t+1})^2}{k^{t+1}} N_I(\mathbf{x}_p^t) N_J(\mathbf{x}_p^t) V_p^{t+1}, \quad (61)$$

$$\mathbf{f}^{int} = - \sum_{p=1}^{n_p} \sum_{I=1}^{n_n} \nabla N_I(\mathbf{x}_p^t) : (\boldsymbol{\sigma}_p^{t+1} - \beta p_p^t \mathbf{I}) V_p^{t+1}, \quad (62)$$

$$\mathbf{f}^{ext} = \sum_{p=1}^{n_p} \sum_{I=1}^{n_n} \rho_p^{t+1} N_I(\mathbf{x}_p^t) \mathbf{b} V_p^{t+1} + \sum_{I=1}^{n_n} \int_{\partial\Omega} N_I(\mathbf{x}_p^t) \mathbf{t} dS, \quad (63)$$

$$\mathbf{f}_f^{int} = - \sum_{p=1}^{n_p} \sum_{I=1}^{n_n} \nabla N_I(\mathbf{x}_p^t) : (-\beta n_{f,p} p_p^t \mathbf{I}) V_p^{t+1}, \quad (64)$$

$$\mathbf{f}_f^{ext} = \sum_{p=1}^{n_p} \sum_{I=1}^{n_n} \bar{\rho}_{f,p}^{t+1} N_I(\mathbf{x}_p^t) \mathbf{b} V_p^{t+1} + \sum_{I=1}^{n_n} \int_{\partial\Omega} N_I(\mathbf{x}_p^t) \mathbf{t}_f dS. \quad (65)$$

Notice that the coefficient matrix in Equation (59) is non-symmetrical, and, in the current work, the least-squares conjugate gradient solver is used to solve the intermediate accelerations.

4.3.5 | Solving pressure Poisson equation

After the nodal intermediate accelerations for the two phases are obtained by solving Equation (59), the next step is to solve the Poisson equation, Equation (38), following the update of intermediate velocity as Equation (37). As the Laplacian matrix \mathbf{L} is symmetric positive definite, a conjugate-gradient-based solver can be used to obtain the nodal incremental pressure. Equation (38) can be rewritten in MPM fashion as:

$$[\mathbf{L}][\hat{p}^{t+1} - \beta \hat{p}^t] = \left[\frac{1}{\Delta t} (\hat{\mathbf{f}} + \hat{\mathbf{f}}_v) \right], \quad (66)$$

$$\mathbf{L} = \sum_{p=1}^{n_p} \sum_{I=1}^{n_n} \sum_{J=1}^{n_n} \left(\frac{n_{s,p}^{t+1}}{\rho_{s,p}^{t+1}} + \frac{n_{f,p}^{t+1}}{\rho_{f,p}^{t+1}} \right) \nabla N_I(\mathbf{x}_p^t) \nabla N_J(\mathbf{x}_p^t) V_p^{t+1}, \quad (67)$$

$$\bar{\mathbf{f}} = - \left[\sum_{p=1}^{n_p} \sum_{I=1}^{n_n} \sum_{J=1}^{n_n} \nabla N_I(\mathbf{x}_p^t) N_J(\mathbf{x}_p^t) V_p^{t+1} \right] \hat{\mathbf{v}}_s^* + \left[\sum_{p=1}^{n_p} \sum_{I=1}^{n_n} \sum_{J=1}^{n_n} \nabla N_I(\mathbf{x}_p^t) N_J(\mathbf{x}_p^t) n_{f,p}^{t+1} V_p^{t+1} \right] (\hat{\mathbf{v}}_f^* - \hat{\mathbf{v}}_s^*), \quad (68)$$

$$\bar{\mathbf{f}}_\nu = \sum_{I=1}^{n_n} \int_{\partial\Omega} N_I(\mathbf{x}_p^t) \left[-n_f(\hat{\mathbf{v}}_f^* - \hat{\mathbf{v}}_s^*) + \Delta t \left(\frac{n_s}{\rho_s} + \frac{n_f}{\rho_f} \right) \nabla(p^{t+1} - \beta p^t) \right] \cdot \mathbf{n} dS. \quad (69)$$

Note that, since the solid grains and pore fluid are assumed to be fully incompressible in the semi-implicit formulation, the phase-specific intrinsic mass density ρ_α is assumed to be constant during the entire simulation, that is, $d\rho_\alpha/dt = 0$.

4.3.6 | Fractional-step correction

As the incremental nodal pressure has been obtained at this stage, the next step is to obtain the correcting accelerations \mathbf{a}^{**} for the solid and liquid phase. Equation (42), can be rewritten in its matrix form as:

$$\begin{bmatrix} \mathbf{M}_s & 0 \\ 0 & \mathbf{M}_f \end{bmatrix} \begin{bmatrix} \hat{\mathbf{a}}_s^{**} \\ \hat{\mathbf{a}}_f^{**} \end{bmatrix} = \begin{bmatrix} \mathbf{G}_s(\hat{p}^{t+1} - \beta \hat{p}^t) \\ \mathbf{G}_f(\hat{p}^{t+1} - \beta \hat{p}^t) \end{bmatrix}, \quad (70)$$

where,

$$\mathbf{G}_\alpha = - \sum_{p=1}^{n_p} \sum_{I=1}^{n_n} \sum_{J=1}^{n_n} n_{\alpha,p}^{t+1} N_I(\mathbf{x}_p^t) \nabla N_J(\mathbf{x}_p^t) V_p^{t+1}. \quad (71)$$

If the lumped-mass matrix is assumed, Equation (70) can be solved explicitly via the mapped nodal mass (48) without any matrix inversion.

4.3.7 | Update of particle kinematics and pressure

At the end of the time step, following the update of nodal acceleration and velocity, Equations (44) and (45), the velocity of material points for the solid and liquid phase are updated from the nodal acceleration (FLIP scheme⁴⁵), whereas the material point positions are updated from nodal solid velocity as:

$$\mathbf{v}_{\alpha,p}^{t+1} = \mathbf{v}_{\alpha,p}^t + \Delta t \sum_{I=1}^{n_n} N_I(\mathbf{x}_p^t) \hat{\mathbf{a}}_{\alpha,I}^{t+1}, \quad (72)$$

$$\mathbf{x}_p^{t+1} = \mathbf{x}_p^t + \Delta t \sum_{I=1}^{n_n} N_I(\mathbf{x}_p^t) \hat{\mathbf{v}}_{s,I}^{t+1}. \quad (73)$$

It is worthy to mention that an alternative variant known as the velocity update scheme is also available in the literature, known as the PIC approach,⁴⁶ which reads

$$\mathbf{v}_{\alpha,p}^{t+1} = \sum_{I=1}^{n_n} N_I(\mathbf{x}_p^t) \hat{\mathbf{v}}_{\alpha,I}^{t+1}. \quad (74)$$

In the subsequent section, the two velocity update schemes, Equations (72) and (74), incorporated in the proposed semi-implicit MPM framework are discussed.

The pore pressure in the material-point level can be updated by mapping the incremental nodal pore-pressure value as:

$$p_p^{t+1} = \beta p_p^t + \sum_{I=1}^{n_n} N_I(\mathbf{x}_p^t)(\hat{p}_I^{t+1} - \beta \hat{p}_I^t). \quad (75)$$

4.4 | Boundary conditions

The material boundary $\partial\Omega$ for the mixture is composed of the Dirichlet ($\partial\Omega_D$) and Neumann ($\partial\Omega_N$) boundaries such that $\partial\Omega_D \cap \partial\Omega_N = \emptyset$ and $\partial\Omega_D \cup \partial\Omega_N = \partial\Omega$. Displacement boundary conditions are applied phase-wise on $\partial\Omega_{\alpha D}$, where $\alpha = s, f$. Here, $\partial\Omega_{fD}$ defines the pore-pressure flow boundary condition, which can overlap or be separated from $\partial\Omega_{sD}$. The intermediate accelerations are also assumed to satisfy the same Dirichlet boundary conditions for fixed prescribed displacement, and lead to

$$\mathbf{a}_\alpha^* = 0 \quad \text{on} \quad \partial\Omega_{\alpha D}. \quad (76)$$

By enforcing boundary condition (76) in Equation (59), the enforced nodal intermediate accelerations \mathbf{a}_α^* and velocities \mathbf{v}_α^* are obtained. Meanwhile, the surface traction \mathbf{t} and phase-wise traction \mathbf{t}_α are acting on $\partial\Omega_N$.

In addition to the displacement or velocity boundary conditions, the elliptic pressure Equation (66) requires a Dirichlet boundary condition for $\phi = (p^{t+1} - \beta p^t)$ on nodes where pressure is prescribed. Similar to the displacement boundary conditions, the prescribed pore pressure can be given as an input. Moreover, if a free-surface problem is involved, a free-surface detection routine^{32,47,48} is used to track the evolution of surface particles. Furthermore, the pressure Poisson equation leads to an artificial boundary force, Equation (69), on $\partial\Omega_v$, which is vague to define. For undrained and drained boundaries, however, the incremental pressure gradient term can be simplified into a homogeneous Neumann boundary condition where $\nabla(p^{t+1} - p^t) \cdot \mathbf{n} = 0$. This can be achieved automatically by enforcing the intermediate normal fluid velocity at the boundary to zero as $\mathbf{v}_f^* \cdot \mathbf{n} = 0$. A recent work by Rosales et al.⁴⁹ shows that a specific reformulation of boundary conditions of the pressure Poisson equation may improve the accuracy up to third order in high-order FEM.

4.5 | Critical time step

The critical time step in the standard explicit MPM formulation is defined by the *Courant-Friedrichs-Levy* (CFL) condition,⁵⁰ and is given by the following equation:

$$\Delta t_{crit,CFL} = \frac{\Delta h_e}{c^p}, \quad (77)$$

where Δh_e is the smallest background element size and c^p is the compressional wave velocity traveling in a medium. In an isotropic poro-elastic continuum body, the compressional wave velocity can be expressed as:

$$c^p = \sqrt{\frac{K + 4G/3}{\rho}}, \quad (78)$$

where $K = K_s$ is the bulk modulus for the solid skeleton, G is the shear modulus, and $\rho = \bar{\rho}_s = n_s \rho_s$ assuming a dry condition. If the porous medium is fully saturated and undrained, then the compression wave velocity expression above should be modified considering the undrained bulk modulus,⁵¹ $K \approx K_u = K_s + K_f/n_f$, and mixture density, $\rho = \bar{\rho}_s + \bar{\rho}_f = n_s \rho_s + n_f \rho_f$.

In the two-phase explicit formulation (see Algorithm 2), the momentum balance of the weakly-compressible fluid is solved separately from the mixture to compute the fluid-phase acceleration \mathbf{a}_f^{t+1} . In this regard, a separate expression of

compressional wave velocity of the pore-fluid phase should be used instead of the one written in Equation (78), such that:

$$c^p = c_f^p = \sqrt{\frac{K_f}{\rho_f}}. \quad (79)$$

In a low soil permeability condition, the above CFL criterion is found to be insufficient to ensure the stability of the explicit two-phase formulation, and thus, as suggested by Mieremet et al.,⁵¹ an additional permeability-dependent stability criterion is considered. Here, a permeability-dependent critical time step derived by Mieremet et al.⁵¹ is used for the explicit MPM simulations, which reads

$$\Delta t_{crit,k} = \frac{-\rho_f g / \rho^m k + \sqrt{(\rho_f g / \rho^m k)^2 + 4\omega^2}}{\omega^2}, \quad (80)$$

with $\omega^2 = 4E/\rho^m(\Delta h_e)^2$ and $\rho^m = \rho + (1/n_f - 2)\rho_f$. In the above expression, E is the solid elastic modulus, k is the permeability in m/s, and $\rho = \bar{\rho}_s + \bar{\rho}_f$ is the mixture density.

Using these critical time step criteria, the critical time step for the explicit MPM can be calculated as:

$$\Delta t_{crit} = \min(\Delta t_{crit,CFL}, \Delta t_{crit,k}). \quad (81)$$

In the proposed semi-implicit scheme, since the stress integration of the solid phase and the evaluation of internal forces are done explicitly at the current configuration t , the selection of critical time step size to ensure the stability condition is still limited by the CFL condition. It is, however, possible to choose permeability-independent time step size due to the implicit evaluation of the drag force assumed in Equation (18). As noted by Markert et al.,³⁸ the time step restriction suggested in the fractional-step method can be partly overcome by taking recourse to staggered implicit-implicit schemes with stabilizing parameters^{30,52,53} or by adding some artificial compressibility to the mixture, which implementation is similar to the modified Chorin-Uzawa method.⁵⁴

5 | NUMERICAL EXAMPLES

This section presents numerical examples demonstrating the performance and efficiency of the proposed semi-implicit MPM algorithm. Detailed comparisons are carried out to present the effect from the method types (explicit and semi-implicit) and fractional-step method types (non-incremental and incremental).

Four numerical examples are presented in the current section. First, the proposed formulation is validated via the classical consolidation problem. The one-dimensional test also is extended to the dynamic regime and a saturated column subjected to cyclic loading is modeled. Then the proposed implementation is also adopted to simulate two-dimensional plane-strain consolidation under different material properties. Finally, a slope landslide triggered by excessive pore pressure is replicated by the proposed MPM extension to showcase its capabilities in solving practical engineering problems. For all numerical examples in this study, a structured mesh is adopted with quadrilateral four-nodes elements with equal order of interpolation function for the kinematic variables and pressure.

5.1 | One-dimensional consolidation

The first case conducted is a one-dimensional consolidation problem, simulated with the proposed semi-implicit coupled formulation and compared with the explicit MPM implementation for porous media. As shown in Figure 2, which depicts the geometry and boundary conditions for the simulation, a saturated granular column is compressed by a constant distributed load $q = 10$ kPa at the top surface, where the pore fluid can drainage freely at the vicinity of the free surface. By default, the column is discretized by 50 elements with element size of $0.02\text{m} \times 0.02\text{m}$. Gravity is neglected in the computation, and zero initial stress and pore pressure are considered. The initial porosity n is set as 0.3 (in our notation, the porosity term n is interchangeable with liquid volume fraction n_f). The soil grain density ρ_s is 2600 kg/m³ and pore water

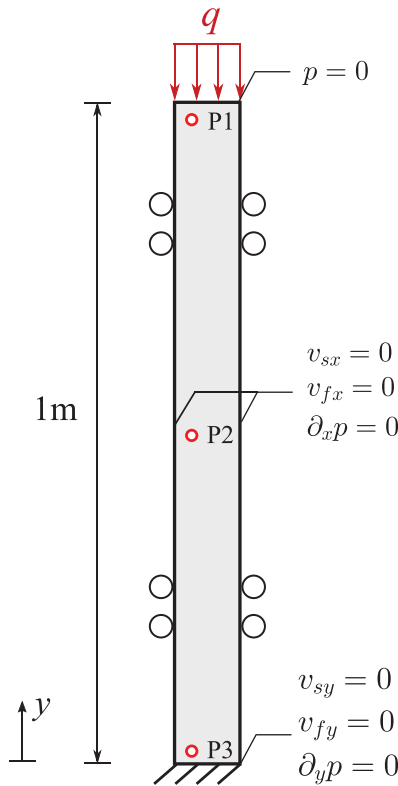


FIGURE 2 Model setup for one-dimensional consolidation

density ρ_f is 1000 kg/m^3 . Isotropic linear elastic constitutive model with Young's modulus $E = 1 \times 10^7 \text{ Pa}$ and Poisson's ratio $\nu = 0.25$ is adopted for the solid phase. Moreover, the fluid phase is assumed to be weakly compressible for explicit MPM and its bulk modulus is set as $K_f = 2.2 \text{ GPa}$, whereas for semi-implicit MPM, the pore-water phase is assumed to be fully incompressible, and thus, the pore pressure is solved implicitly by a projection scheme.

5.1.1 | High-permeable material

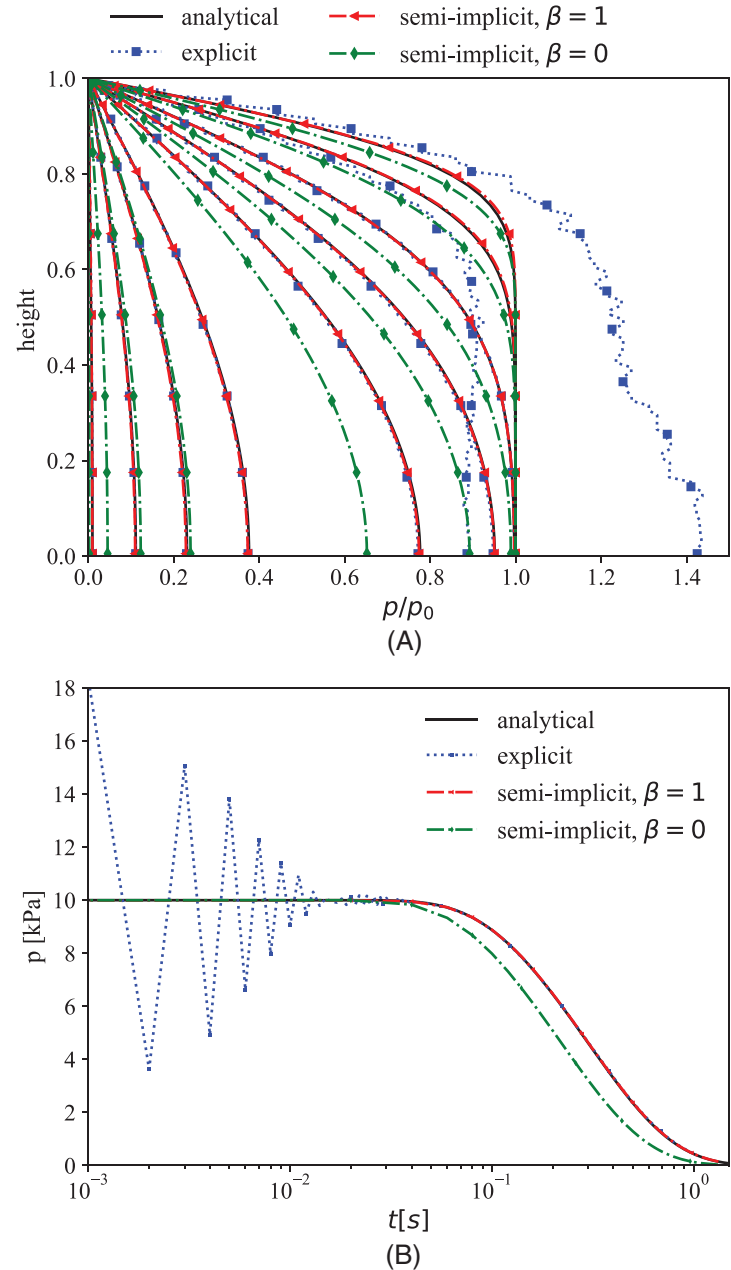
Firstly, the case of relatively high permeability with $k = 1 \times 10^{-3} \text{ m/s}$. In order to ensure the stability of the computation, time step Δt for explicit MPM is set to be $1 \times 10^{-5} \text{ s}$, while for semi-implicit MPM (both incremental form and non-incremental form), the time step size is chosen as $2 \times 10^{-4} \text{ s}$. The analytical solution from Terzaghi's consolidation theory⁵⁵ is used to validate the results obtained from the numerical simulations. A dimensionless time T is used for following discussion, which is defined as

$$T = c_v \frac{t}{H^2} = \frac{k m_v}{\rho_f g} \frac{t}{H^2}, \quad (82)$$

where $H = 1 \text{ m}$ is the height of the column, c_v is the coefficient of consolidation and m_v is the constrained modulus of solid phase.

Figure 3A shows the pore-pressure profile obtained along the column at various time instances, that is, $T = 0.01, 0.02, 0.05, 0.1, 0.2, 0.5, 0.7, 1.0,$ and 2.0 . From the presented comparison, it is clear that the explicit and semi-implicit MPM based on the incremental fractional step, that is, $\beta = 1$, agrees well with the theoretical prediction although there is a considerably large discrepancy for the explicit one, particularly during the initial stages. On the contrary, the semi-implicit MPM solution based on the non-incremental fractional-step method, that is, $\beta = 0$, renders a faster dissipation of pore pressure. This error is induced from the form of splitting the momentum equations. As seen from Equation (19), for the case of non-incremental fractional step method ($\beta = 0$), no pore-pressure term at any time instance is involved in computing the intermediate accelerations. This absence of pore pressure leads to erroneous interaction force between the solid skeleton

FIGURE 3 One-dimensional consolidation results: (A) pore-pressure profile along the column for $T = 0.01, 0.02, 0.05, 0.1, 0.2, 0.5, 0.7, 1.0,$ and 2.0 (B) pore-pressure evolution at the bottom of the soil column



and pore fluid, and thus a poor estimation of the intermediate acceleration. Consequently, this erroneous intermediate acceleration cannot be corrected to the precise solution by the correction step, causing the error to accumulate.

The history of the pore pressure at the bottom for different methods is extracted and the result is plotted in Figure 3B. As can be observed, there is an oscillation in the explicit MPM, especially at the first several steps of the computation. The dissipation then can go through a steady change after it goes to an equilibrium stage. On the other hand, the semi-implicit MPM presents a much smoother curve during the whole consolidation process. Again the semi-implicit MPM based on the non-incremental fractional-step method ($\beta = 0$) yields a faster dissipation of pore pressure. Furthermore, the accuracy of the incremental fractional step method is supported by Figure 4 which measures the relative error e_r of pore pressure at the bottom of the column upon mesh refinement at $T = 0.5$. As piecewise linear basis function is used, linear convergence of the truncation error is expected for this particular example with small deformation. It is important to note, however, that the accuracy of the integration is subjected to degradation as particles move through the background elements, as discussed by Steffen et al.⁵⁶ Considering these aspects, the semi-implicit MPM based on the incremental fractional step, $\beta = 1$, is preferred and adopted for the rest of the numerical examples in this study. The semi-implicit MPM term is used to denote the incremental form for the sake of conciseness hereafter.

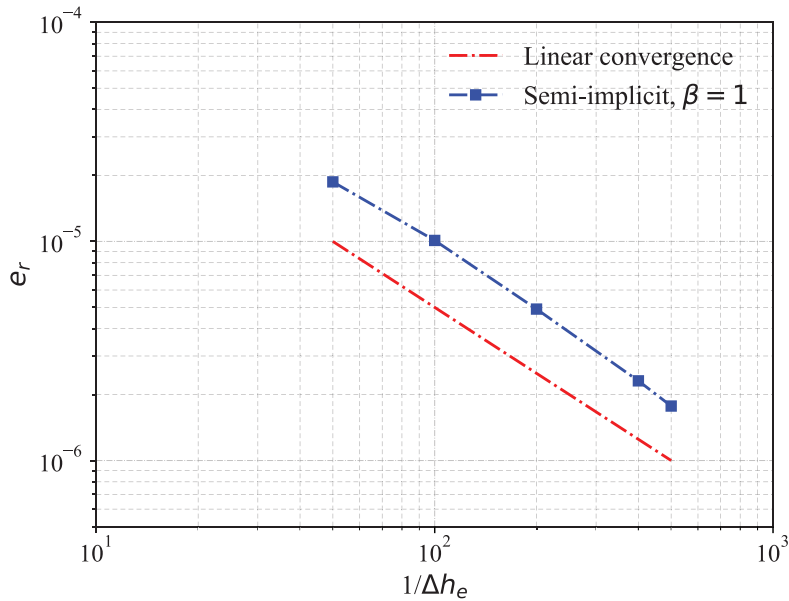


FIGURE 4 Convergence plot of the relative error $e_r = |(p_{\text{MPM}} - p_{\text{analytical}})/p_{\text{analytical}}|$ of the pore-pressure at the bottom of the soil column compared to the analytical solution. The proposed incremental fractional-step semi-implicit scheme with $\beta = 1$ exhibits linear convergence upon mesh-refinement

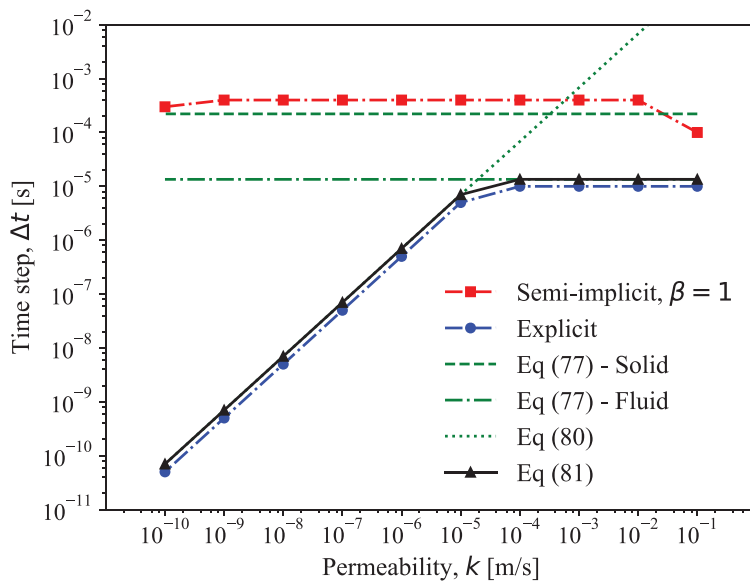


FIGURE 5 Critical time steps for explicit and semi-implicit MPM under different permeability conditions. The element size is 0.02×0.02 m and the bulk modulus for fluid phase in explicit MPM is 2.2 GPa

5.1.2 | Medium to low-permeable material

Despite both of the explicit and semi-implicit MPM giving correct results under high-permeable conditions, the advantage of the proposed method can be demonstrated when the permeability reduces to a lower level. A sensitivity analysis is carried out to evaluate the critical time steps for the explicit MPM and the proposed semi-implicit MPM considering different permeability values. The model setup in this sensitivity analysis is the same as the previous case, except the permeability value k is varied. Here, the maximum time step is obtained for each permeability case such that it can ensure the stability of the computation. This sensitivity analysis covers a wide range of permeable conditions, ranging from nearly undrained condition $k = 10^{-10}$ m/s to highly drained condition $k = 10^{-1}$ m/s. The measured critical time steps are depicted in Figure 5 along with the critical time step determined analytically, which were given previously in Equations (77)–(81).

For the explicit MPM formulation, the critical time step remains stable under highly-permeable conditions ($k > 10^{-3}$ m/s) as it is mainly dominated by the CFL condition of the fluid phase. However, as the permeability reduces, the critical time for the explicit scheme also drops correspondingly at the same rate as the permeability, which results in an extremely small time step for the nearly impermeable material. On the other hand, the critical time step for semi-implicit MPM appears to be free of the limitation on permeability. Over the whole regime of permeability, the critical time step remains at the order of $\Delta t \sim 10^{-4}$ s, which is at least one order higher than that of the explicit case. Despite the fact that the

FIGURE 6 Pore-pressure dissipation at the bottom of the column under different permeabilities in one-dimensional consolidation problem

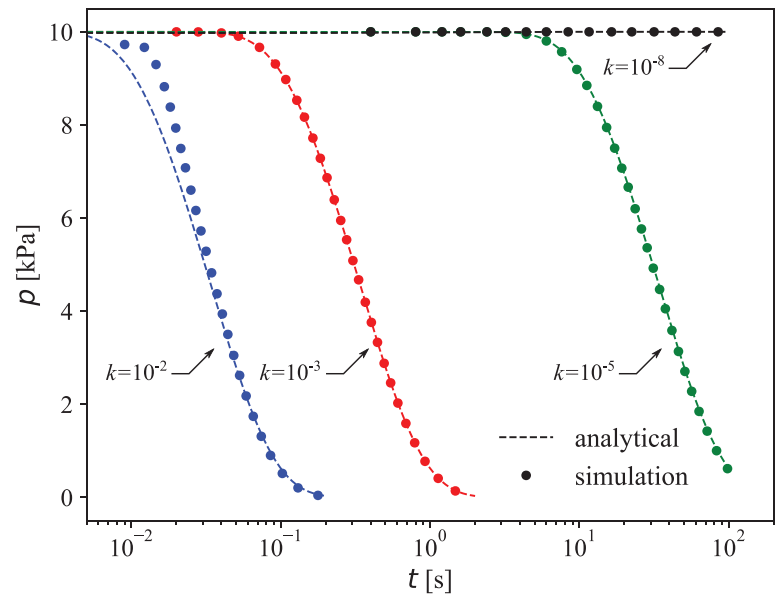
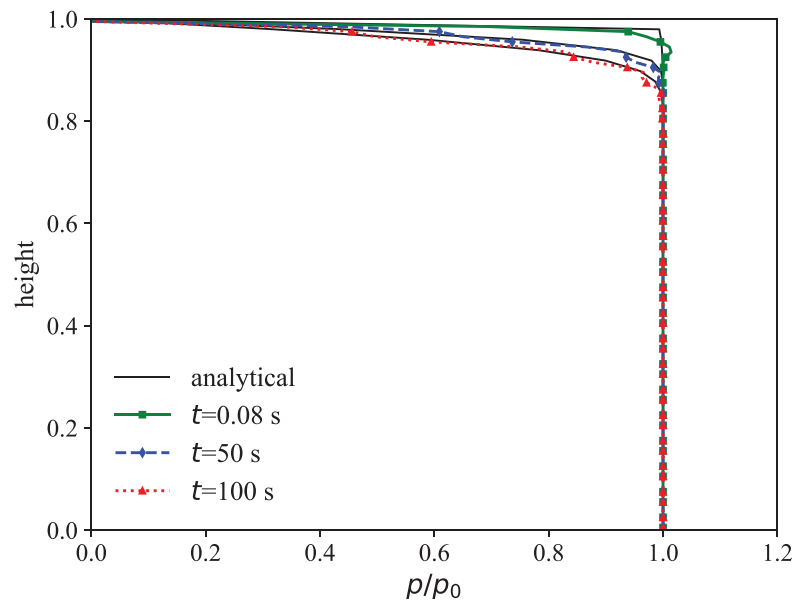


FIGURE 7 Pore pressure along the granular column for case of $k = 10^{-8}$ m/s at different time instances: $t = 0.08$ s, 50 s, 100 s



proposed scheme is more computationally expensive than the explicit formulation to perform a single time advancing step, it allows significantly larger time increment and less number of steps in total to perform practical simulations. This feature, therefore, facilitates more effective modeling of hydro-mechanical coupled systems, particularly for problems involving low permeability.

To outline the influence of permeability on the pore-pressure dissipation process, the one-dimensional consolidation simulation is repeated with varying permeability, namely $k = 10^{-2}$, 10^{-3} , 10^{-5} , and 10^{-8} m/s. The results of pore-pressure dissipation at the bottom of the column are presented in Figure 6. The proposed semi-implicit MPM yields a stable pore-pressure evolution without extra oscillations, and gives correct results in all computations. Figure 7 shows the results of the pore pressure along the column in the case of $k = 1 \times 10^{-8}$ m/s. In the initial stage of the consolidation, a mild pore-pressure oscillation appears at the drainage surface. Similar behavior is also reported²⁶ and is attributed to an inherent pitfall of the Galerkin interpolation. Due to the low permeability used, only a little reduction is formed at the top, the free surface namely, and most of the column can keep a constant pore pressure with no dissipation.

In the current work, since the drag force term is computed from the intermediate velocities which require the unknown intermediate acceleration terms (see Equation (18)), the time-step dependency on the permeability coefficient k is significantly reduced. However, it should be noted that the accuracy of the proposed projection-based coupling scheme still has

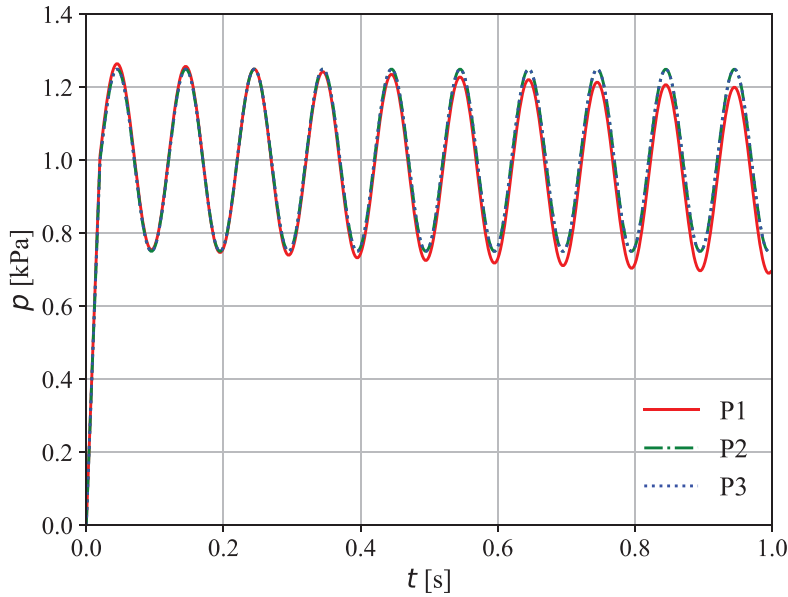


FIGURE 8 Pore-pressure evolution for selected points in case of semi-implicit MPM

a slight dependency on the size of Δt as the intermediate velocities used to compute the drag force is not an actual discrete velocity that satisfies the mixture mass-balance equation with pore-fluid incompressibility constraint.

5.2 | One-dimensional column under cyclic loading

While the proposed semi-implicit MPM formulation is verified previously for a quasi-static consolidation example, its performance to simulate dynamic hydro-mechanical coupled problems is also investigated. In this subsection, the simulation of a one-dimensional column subjected to cyclic loading is conducted, following that in Li et al.⁴⁰ The geometry and the boundary conditions are the same as the one presented in the one-dimensional consolidation problem (Figure 2). The solid phase is again assumed as linear elastic material with Young's modulus $E = 1 \times 10^7$ Pa and Poisson ratio $\nu = 0.2$. The initial porosity n for the mixture is set as 0.3. The soil grain density ρ_s is 2600 kg/m^3 and pore water density ρ_f is 1000 kg/m^3 . In Li et al.,⁴⁰ the permeability is taken as zero to reproduce the fully undrained condition. However, a relatively small permeability $k = 1 \times 10^{-7}$ m/s is selected in this study for facilitating the explicit MPM computation whose the critical time step is restricted by the permeability. The time step $\Delta t = 1 \times 10^{-4}$ s for semi-implicit MPM and $\Delta t = 1 \times 10^{-8}$ s for explicit MPM were selected. The cyclic loading $q(t)$ (unit in kPa) acting on the top surface of the column is defined as follows

$$q(t) = \begin{cases} t/0.02 & t \leq 0.02\text{s}, \\ 1 + 0.25 \sin(20\pi(t - 0.02)) & \text{otherwise.} \end{cases} \quad (83)$$

The simulation duration for semi-implicit MPM is 1 s, while that for the explicit MPM is only 0.1 s due to the extremely small time step size employed. Three particles, namely P1, P2, and P3, are chosen for monitoring the response pore pressure and their positions are marked in Figure 2.

The result obtained from the semi-implicit MPM is depicted in Figure 8. It appears that the curves corresponding to P2 and P3 overlap completely, indicating an identical response for the lower half of the column when subjected to the cyclic load. Yet there is a minor discrepancy between P1 and the other two monitoring points. In the first few loading cycles, the peak pore pressure for P1 is slightly larger because of the initial overshoot of pressure near the top surface (see the discussion in the last subsection). Due to the dissipation of the pore pressure, especially for the soil close to the drainage boundary, the peak pore pressure for P1 also reduces generally and is smaller than that for P2 and P3 at the end of the computation.

Figure 9 presents the comparison of results during the first 0.1 s for different MPM formulations. Again it is clear that the semi-implicit MPM offers stable and smooth results for all selected points. Conversely, albeit generally capturing the rational pore-pressure responses, the explicit MPM yields a result with moderate fluctuation which is more apparent for

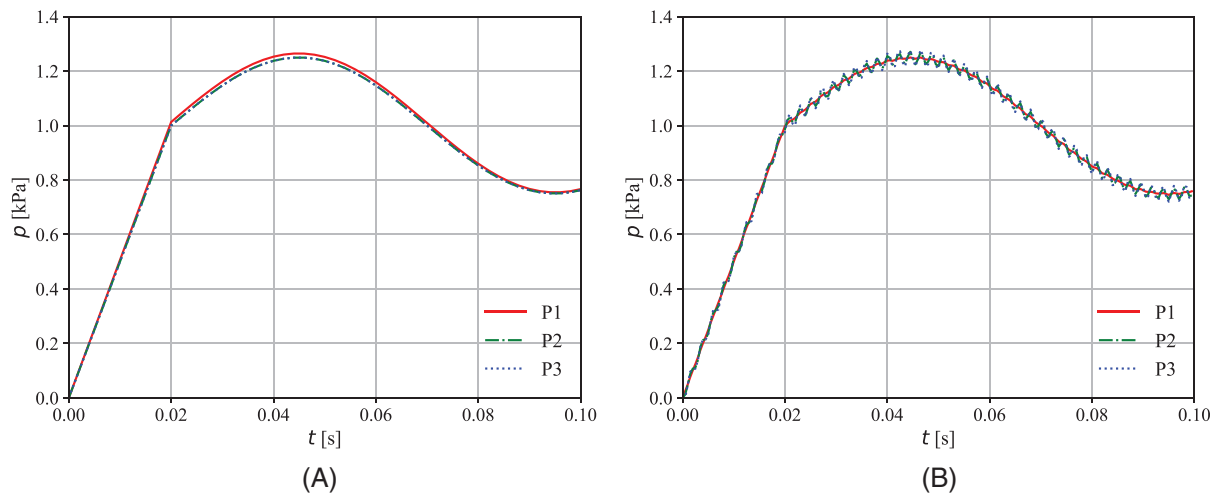
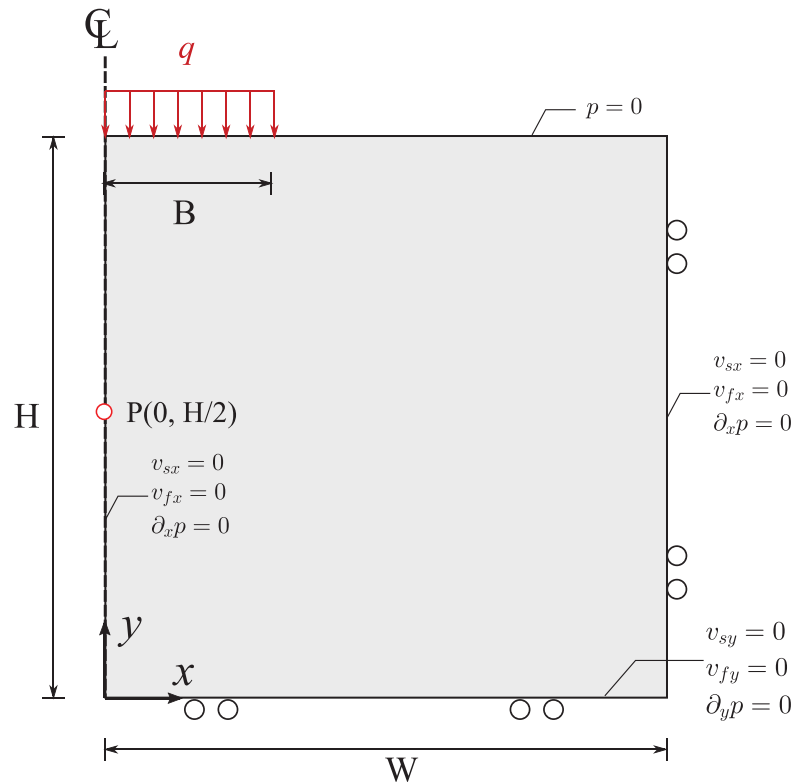


FIGURE 9 Comparison of the response during the first 0.1 s. (A) semi-implicit MPM, (B) explicit MPM

FIGURE 10 Model setup for two-dimensional consolidation problem



the lower half of the problem domain. This dynamic numerical example reveals that the proposed semi-implicit based on $\mathbf{u} - \mathbf{v} - p$ formulation⁸ can not only handle the ordinarily quasi-static problem but also cope with the complex dynamic problem for saturated porous media.

5.3 | Two-dimensional consolidation

A two-dimensional consolidation test under plane strain condition is simulated to further investigate the performance of the proposed method. The geometry of the problem is shown in Figure 10. Only half of the problem domain is modeled by the symmetric nature of the problem. The fully saturated soil domain possesses a dimension of 10×10 m ($W \times H$), and is discretized by quadrilateral elements with element size of 0.5 m and 4 particles per cell (PPC). A constant load acting at the ground surface, $q = 20$ kPa, spans a length of $B = 3$ m. Gravity is neglected for this case, and initial stresses and pore

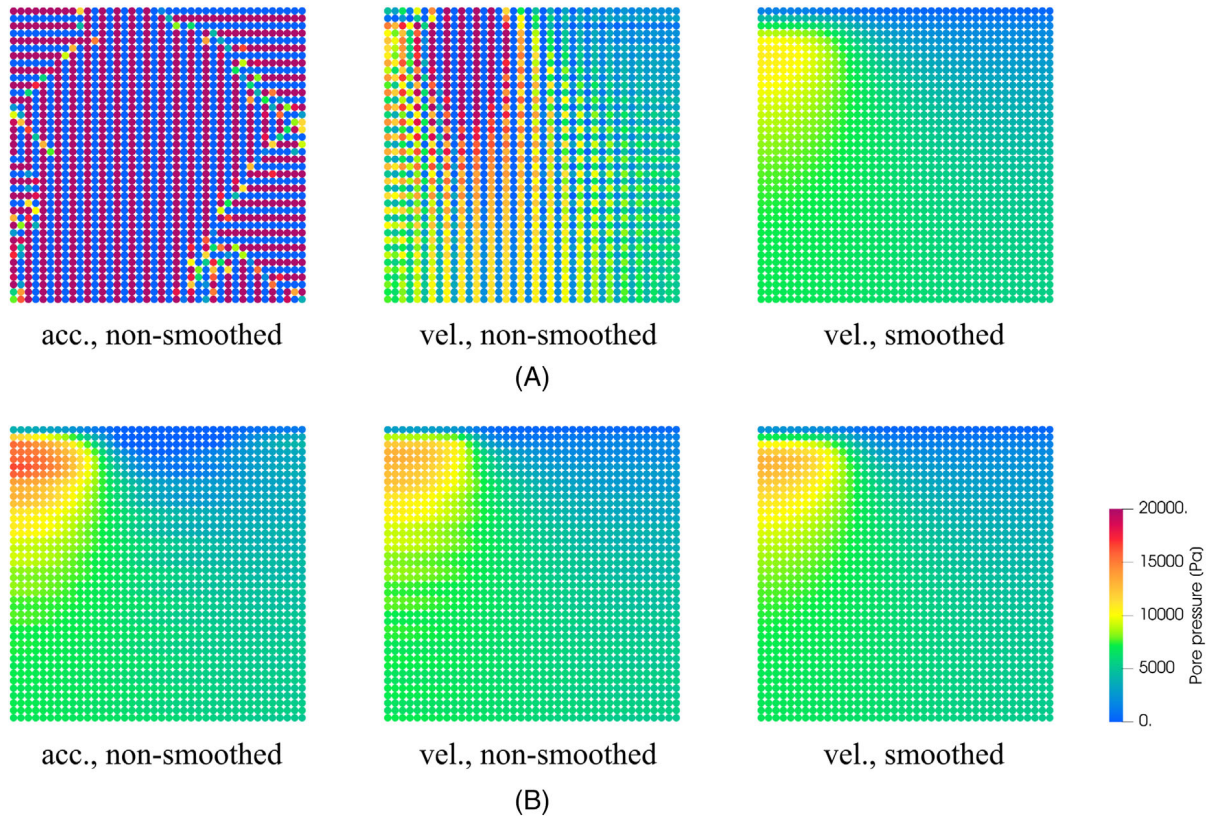


FIGURE 11 Pore-pressure contour using different velocity updated schemes and pore-pressure smoothing technique at $t = 0.1$ s, $\nu = 0$: (A) explicit MPM, (B) semi-implicit MPM

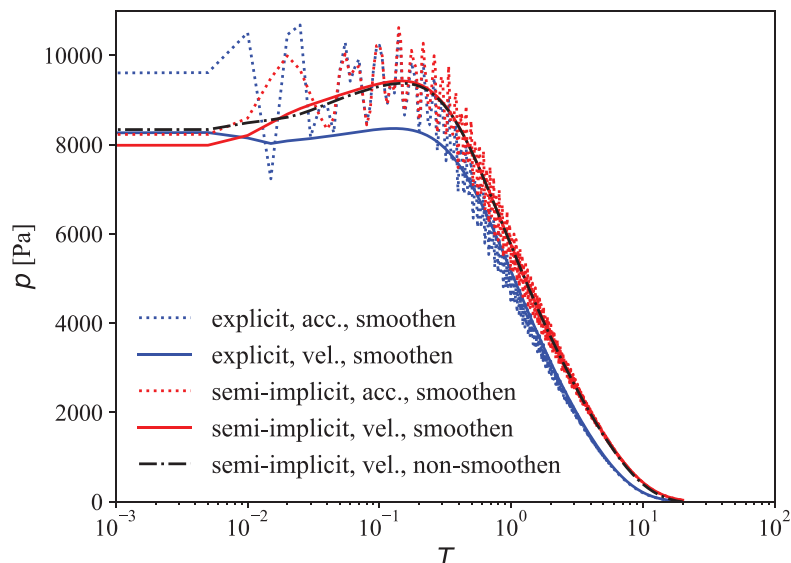
pressures are zero therefore. The initial porosity is set as $n = 0.3$, grain density is set as $\rho_s = 2600 \text{ kg/m}^3$ and fluid density is set as $\rho_f = 1000 \text{ kg/m}^3$. The solid phase is assumed to be isotropic linear elastic. Young's modulus is set as $E = 1 \times 10^7 \text{ Pa}$ and Poisson ratio is varying from 0 to 0.4 for the parametric study. The bulk modulus for fluid phase, which is used in explicit MPM, is $K_f = 2.2 \times 10^9 \text{ Pa}$. The time steps are $\Delta t = 2 \times 10^{-4} \text{ s}$ and $\Delta t = 2 \times 10^{-5} \text{ s}$ for semi-implicit and explicit MPM, respectively, whereas the total simulation time is set to be 200 s.

Firstly, the influence of different velocity update schemes is investigated. In MPM, two schemes are commonly adopted to update the particle velocities, namely the *acceleration update* and *velocity update*, also termed as FLIP and PIC scheme in the literature.^{45,57,58} For the velocity update scheme, particle velocities are overwritten by the interpolated velocity from the background nodes, generally leading to a more stable computation but extensive energy dissipation. While for the acceleration update, the particle velocity is incremented by the acceleration mapped from the nodes. It maintains better energy conservation. However, it also suffers from more numerical noise,^{42,58} which might build up over time depends on the time integration scheme assumed. While only the acceleration update has been used in the one-dimensional consolidation cases, both of the two update methods are considered here to study its influence on the results.

Figure 11 depicts the pore-pressure contours for the semi-implicit and the explicit MPM using various velocity update schemes at $t = 0.1$ s. The explicit MPM with an acceleration update yields a spurious pore-pressure field with significant numerical oscillation. Though the explicit MPM can offer a better pore-pressure contour via the velocity update scheme, the oscillation near the loading boundary still exists. This numerical oscillation causes a build-up of instability that grows over time, causing the computation could not be completed even though with a smaller time step, for example, $1 \times 10^{-7} \text{ s}$. It is worth noting that this oscillation originates from the inherent instability of the algorithm, rather than the well-known cell-crossing noise of MPM since the applied load is low in magnitude and the deformation is small. On the other hand, the proposed semi-implicit MPM is free of such oscillation, offering a smooth and stable pressure distribution for both the acceleration and the velocity update schemes.

When equal order interpolation is employed for the discretization of kinematic variables and pore pressure, the fractional-step method can provide more stable results free of inf-sup instability. As discussed by Bandara et al.,¹⁹ it is common to apply numerical stabilization techniques in the explicit MPM, such as the reduced integration technique or

FIGURE 12 Pore-pressure evolution at point P using different velocity updated schemes and pore-pressure smoothing technique, $\nu = 0$



the B-bar approach, to avoid spurious pressure field. Herein, a simpler post-extrapolation of pore pressure is adopted. By mapping the pore pressure from the material points to the background node and extrapolating the nodal pore pressure back to the material point, the pressure oscillation can be filtered and smoothed, and therefore, yielding to more stable results. This scheme is effective as manifested in the smoothed contour shown in Figure 11A (right).

An observation point, $P(0, H/2)$, located at the mid-depth of the center-line is selected to present the pore-pressure dissipation results. Figure 12 shows the obtained pore-pressure results by the explicit and semi-implicit MPM with different velocity update schemes. The pore-pressure evolution is plotted against a dimensionless time $T = c_v t / B^2$, where c_v is the coefficient of consolidation defined in Equation (82). Here, the pressure smoothing technique is employed for the explicit schemes as the results without smoothing is too spurious and hardly meaningful for comparison. When it comes to the acceleration update scheme, the pore pressure displayed certain fluctuation mainly because of the repeated reflection of the pressure wave from the surrounding boundaries. The velocity update can eliminate the oscillation effectively by damping the velocity field without altering the consolidation process as indicated by two converged curves. Additionally, the explicit MPM results show a significant damping effect, and thus, the pore pressure is dissipated faster than the semi-implicit one. Moreover, the smooth and non-smooth result for the semi-implicit MPM shows that the pressure smoothing technique does not alter the obtained results.

It is also interesting to note that, there is a slight increase in pore pressure during the consolidation process. This behavior is well known as the Mandel-Cryer effect,^{59,60} which is a typical phenomenon in two and three-dimensional consolidation problems and is affected by various factors, for example, soil geometry, permeability, and material properties. Here, the effect of different Poisson ratio ν is investigated and the result is plotted in Figure 13. The maximum increase of pore pressure is produced by the case with zero Poisson's ratio, which indicates that the Mandel-Cryer effect decreases with increasing ν .

5.4 | Slope failure

A problem of slope failure is adopted to test the method's performance towards practical geotechnical engineering problems. Here, the well-known Selborne landslide experiment^{61,62} is simulated as a case study since it provided sufficient field monitoring data. The purpose of the current test is to investigate the progressive failure mechanism induced by excessive pore pressure. Numerical works on this case have been conducted based on the explicit MPM,^{24,63} where the permeability used in the model is many orders higher than the real value to obtain a stable result and reduce the computation time. Here, with the semi-implicit MPM, a wider range of permeability conditions can be adopted and this is benefited from the fractional-step scheme.

Figure 14A illustrates the problem geometry as well as the soil profile. The original ground is excavated as a 2:1 slope with the length of 18 m before the test. The ground mainly consists of six layers, while it is simplified into two layers including the weathered and the unweathered clay in the MPM model, as shown in Figure 14B. Only the free-surface

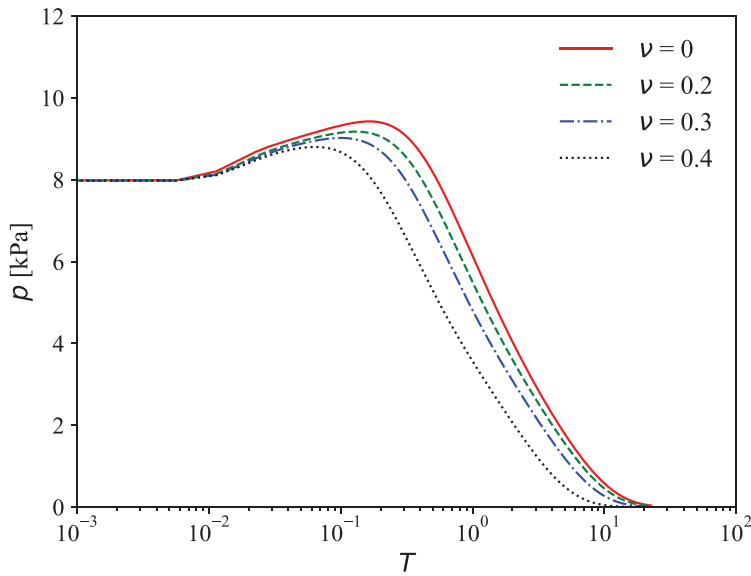


FIGURE 13 Comparison of pressure history at point P for different Poisson ratio values

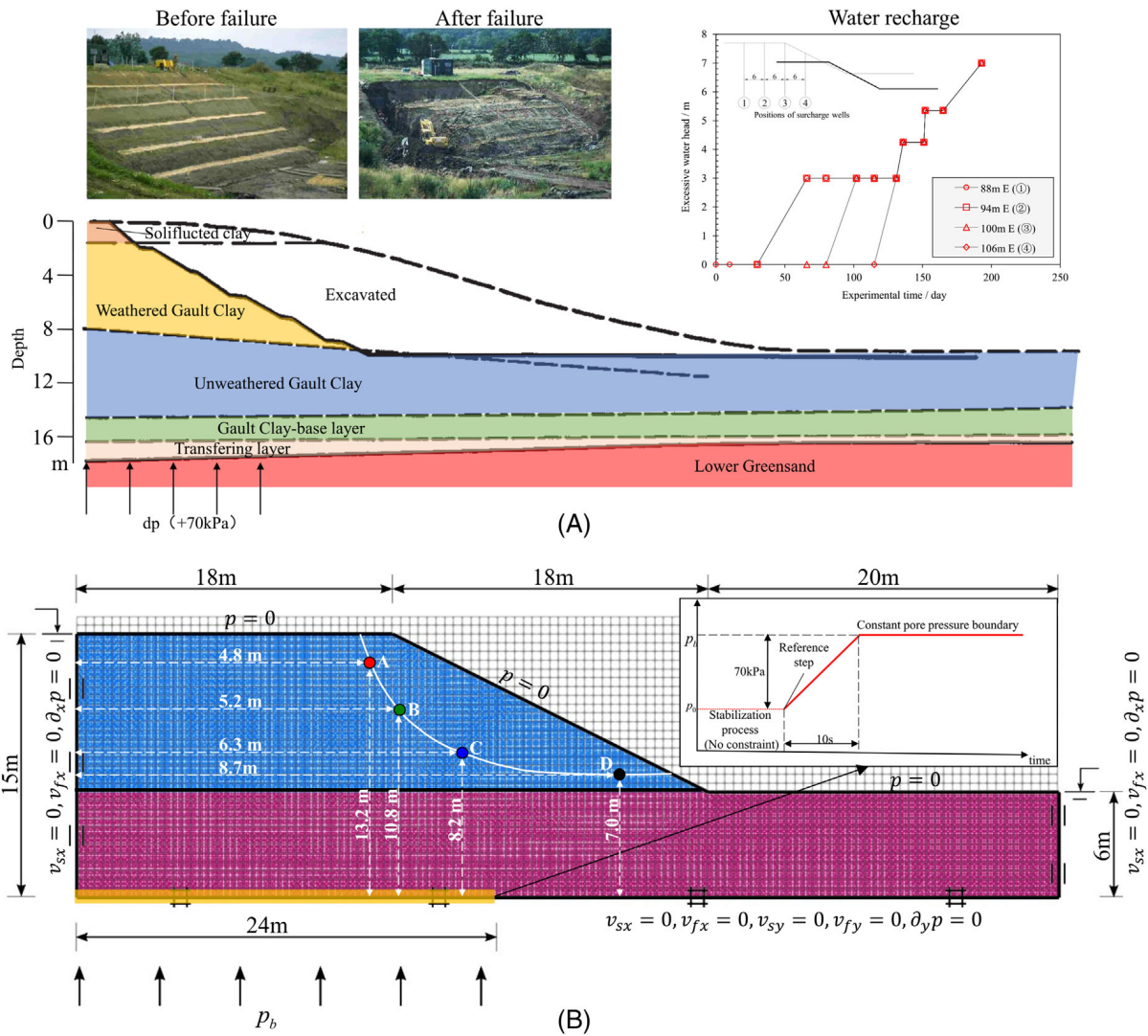


FIGURE 14 Illustration of the slope model: (A) geometry of the Selborne landslide,⁶⁴ (B) the considered MPM model

TABLE 2 Simulation parameters for MPM control in the slope failure problem

Parameters	Symbol	Value
Time step	Δt (s)	0.001
Size of cell	Δh_e (m)	0.5
Total number of nodes	n_n	3729
Particles per cell	PPC	4×4
Total number of particles	n_p	37056

layer is permeable, whereas the other boundaries are impervious. At the beginning of the simulation, a pseudo water table is set at the soil surface as an initial condition. With this setting, we can obtain compatible and smooth initial stress and pore pressure fields through a certain stabilization period. The other simulation parameters are shown in Table 2.

After the stabilization period, the water table previously defined is removed, and an excessive pore pressure is loaded from four surcharge wells located in the slope as shown in the insertion of Figure 14A to raise the water head by 7 m gradually (in 196 days), which then induces the slope failure. The displacements and pore pressures at different positions were recorded during the whole process where the beginning day of the water recharge is defined as the 0th day. According to the monitoring results, an apparent displacement increment is caught at the 170th day and it increased to the engineering failure level at the 184th day. The final obvious landslide is observed at day 193 as reported by Cooper et al.,⁶² which means that the stability is broken during the water recharge.

As the proposed formulation adopts an explicit scheme for stress integration, it is still considered difficult to perform a real-time simulation of the experiment for a period of 200 days. In the current study, it is aimed to reduce the diffusion time of the excess pore pressure from the bottom to the top by defining a considerably large initial permeability ($k = 1 \times 10^{-3}$ m/s). As the permeability condition of the soil is isotropic and uniform, the propagation behaviors before the collapse should be almost the same except the time needed to reach the slope failure.

A linear incremental pore-pressure boundary constraint is applied to the nodes at the specified part of the bottom left boundary, denoted as p_b in Figure 14B. Here, the pore-pressure constraint profile can be divided into three main stages. First, a reference step is predefined and no treatment is necessary before this step is reached. Then the pore-pressure values at the specified nodes are recorded at the predefined reference step and set as the initial pore-pressure condition. In the second stage, the pore-pressure profile increases linearly during the period of 10 s with a final pore-pressure value of about 70 kPa (7 m-water-head) larger in comparison to the initial condition. Finally, the pore-pressure constraints are kept constant until the end of the simulation, and this is denoted as the third stage of the boundary condition. The simulation is carried out until an obvious failure phenomenon is caught in the slope, where the acceleration profile is used as the indicator for the beginning of the slope movement.

A stabilization period is first carried out assuming a linear-elastic model to obtain the initial stress and pore-pressure field. Then the soil material model is changed to a Mohr-Coulomb model with linear strain-softening depending on the accumulated plastic deviatoric strain ϵ_d^p , which can capture the behavior of progressive failure as suggested by Robert.⁶⁵ The material parameters assumed in the current problem are presented in Table 3, which are obtained from the published investigations.^{61,62} The soil permeability will be firstly set as 1×10^{-3} m/s for all the cases before the slope collapse. Then, a range of permeability coefficient k , from $1 \times 10^{-8} \sim 1 \times 10^{-3}$ m/s, is simulated to study its effect on the evolution of failure. It should be noted that, the real value of the permeability coefficient k in the experiment⁶² was recorded to be about $4 \times 10^{-9} \sim 5 \times 10^{-8}$ m/s.

Figure 15 presents a series of contours of the plastic deviatoric strains, excess pore pressures, and effective vertical stresses, which were obtained from the case with permeability $k = 1 \times 10^{-3}$ m/s. Here, the time indicated in the figures is set according to the start of water recharge. The trend of the landslide appears during the recharge and a quasi-circular shear band is formed gradually, which is similar to the experimental observation. Because of the large strength of the lower soil layer, the displacement of the slope toe is almost horizontal, and thus, causing the landslide only to exist in the weathered upper soil layer. The stress concentration appears at the toe firstly and induces the formation of the shear band.

The excess pore pressure shown in Figure 15 (center) is computed as the difference between the current pore-pressure value and the pore-pressure value at the start of water recharge. As the initial permeability used is relatively large, the

TABLE 3 Soil parameters in the slope failure simulation

Property	Symbol	Soil type	
		Upper layer	Lower layer
Young's modulus	E (kPa)	20000	20000
Poisson ratio	ν	0.3	0.3
Soil grain density	ρ_s (kg/m ³)	2000	2000
Fluid density	ρ_f [kg/m ³]	1000	1000
Initial porosity	n	0.3	0.3
Permeability	k (m/s)	$10^{-3} \sim 10^{-8}$	$10^{-3} \sim 10^{-8}$
Peak friction angle	φ_p [°]	24	26
Residual friction angle	φ_r [°]	13	15
Peak cohesion	c_p (kPa)	15	25
Residual cohesion	c_r (kPa)	0.5	0.5
Peak plastic deviatoric strain	ε_p^{plas}	0	0
Residual plastic deviatoric strain	ε_r^{plas}	0.1	0.1

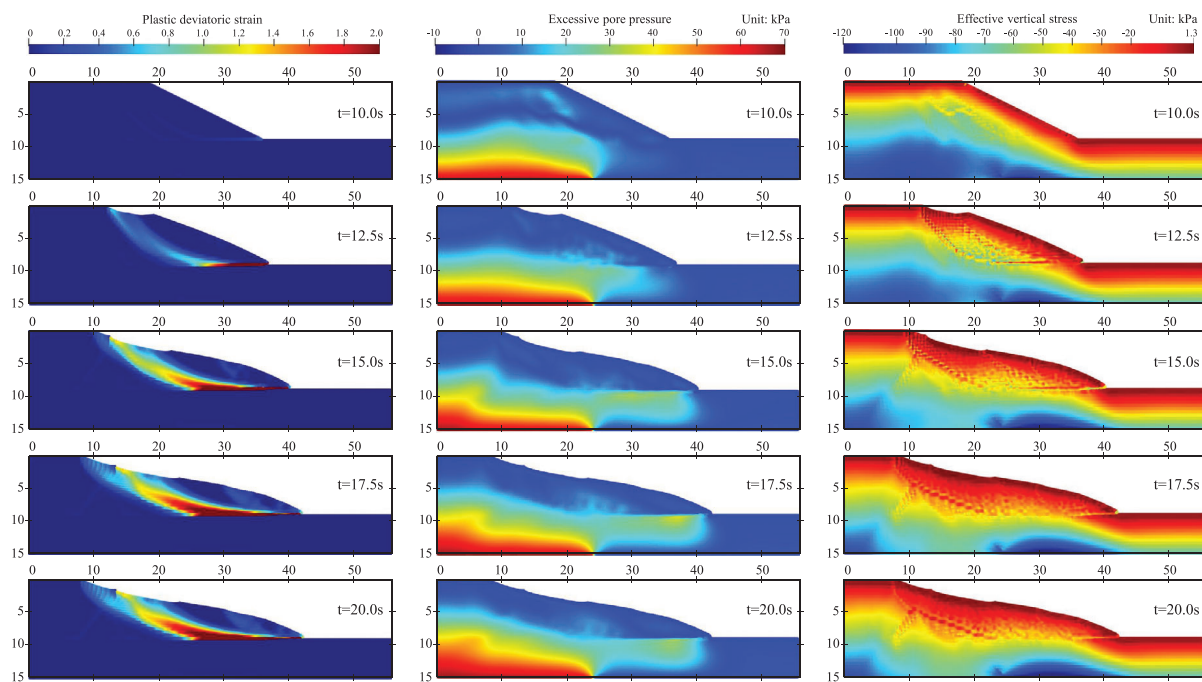


FIGURE 15 Contours of the slope model results: (left) plastic deviatoric strain, (center) excessive pore pressure, and (right) effective vertical stress

propagation of pore pressure is fast and it is transferred to the upper part of the slope quite uniformly before the failure is initiated. Furthermore, during the collapse, as the extension deformation in the moving block causes the volume of soil element to dilate, a negative increment of pore pressure in the slope is observed. Correspondingly, an increase of pore pressure can be seen below the moving block, which is caused by the loading exerted by the block's self-weight. Meanwhile, as shown in Figure 15 (right), the vertical effective stress reduces gradually during the upheaval of the water level. An obvious unloading process appears when the collapse occurs, which is caused by the movement of the soil (x coordinate 10–20 m in Figure 15). This also contributes to the increase in the vertical stress below the moving block (x coordinate 25–40 m in Figure 15).

To investigate the effect of soil permeability, the velocity magnitudes along the failure slope in different permeability conditions are compared as shown in Figure 16. The positions of four observation points, A ~ D, were determined earlier, as shown in Figure 14B, which were selected along the failure curve observed in the experiment conducted by Cooper et al.⁶²

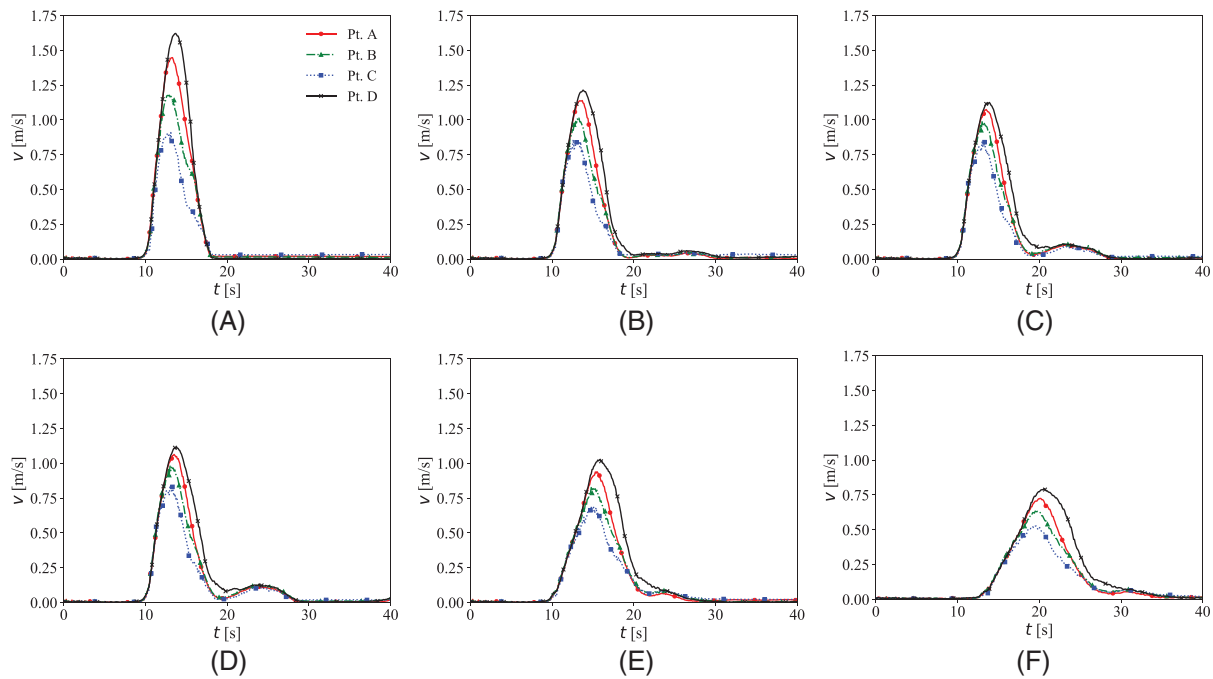
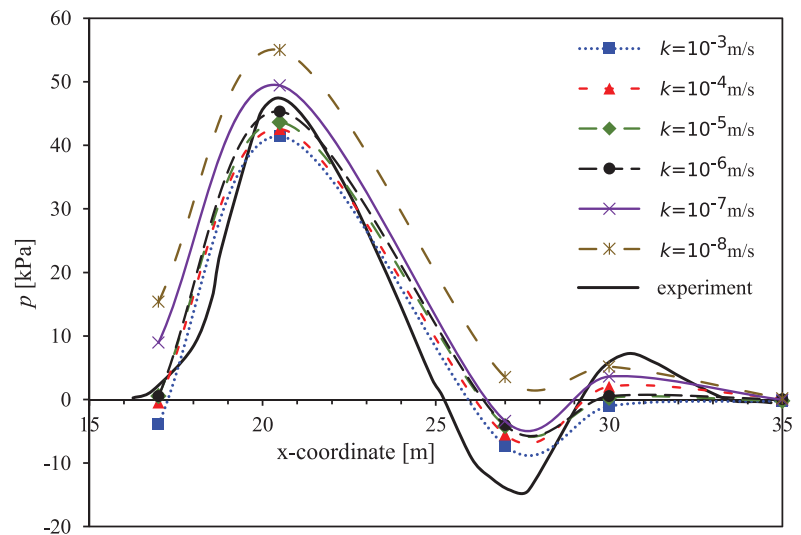


FIGURE 16 Velocities of positions along the shear band: different permeabilities (A) $k = 1 \times 10^{-3}$ m/s, (B) $k = 1 \times 10^{-4}$ m/s, (C) $k = 1 \times 10^{-5}$ m/s, (D) $k = 1 \times 10^{-6}$ m/s, (E) $k = 1 \times 10^{-7}$ m/s, (F) $k = 1 \times 10^{-8}$ m/s

FIGURE 17 Pore pressure along the shear band right before the occurrence of the failure (the simulation results are plotted at $t = 10$ s, while the experimental data⁶² is measured at day 184)



The obtained numerical results showed in Figure 16 indicate that the collapse starts earlier than the end of the water recharge at 10 s. As a large permeability is used for all cases before the failure happens, the initial velocity condition is expected to be the same with almost zero magnitudes. Although the shear band is initiated at the slope toe at the beginning of the failure (see Figure 15), the difference of initiation time observed at the four observation points is relatively small. This behavior is identical to the experimental result. The velocity of the toe observed at point D is always larger than the other points. This results in an extension deformation in the moving block, which is in accordance with the presented pore-pressure results.

With the reduction of permeability, the dissipation of excess pore pressure becomes slower, where the maximum velocity also decreases. Hence the degradation of the shear strength during the collapse requires a longer time, widening the time needed for the motion to stop. This phenomenon is related to the increase of the drag force, which prevents the development of the fluid relative velocity, and correspondingly slows down the diffusion of the excess pore pressure.

Figure 17 shows the pore-pressure values along the shear band right before the occurrence of the failure. Here, the experimental data is obtained from an interpolated cross section on the center-line of the slip mass.⁶² In the obtained

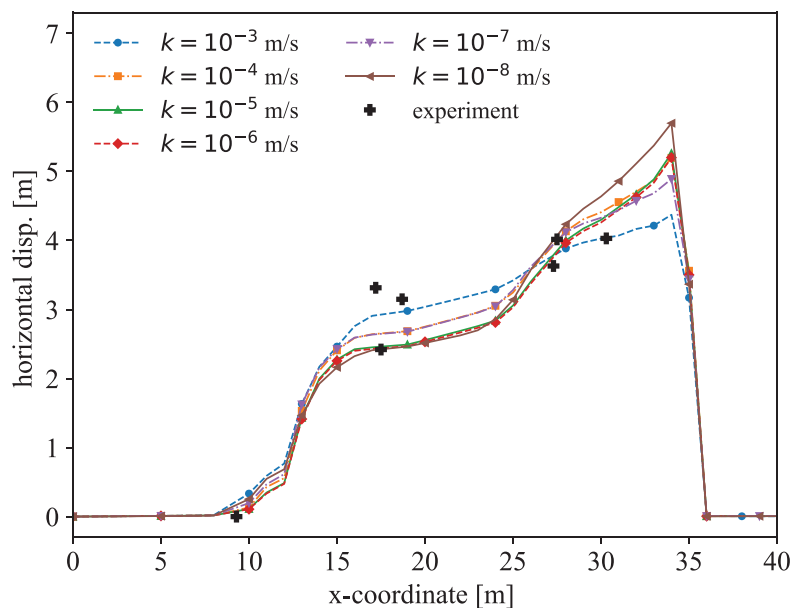


FIGURE 18 Horizontal displacement of the slope surface at final state

results, all cases of different permeability value can capture a similar tendency as the measured experimental data. As mentioned earlier, the low permeability slows down the pore-pressure dissipation rate, and thus, a larger pore-pressure value along the shear band is generated. Furthermore, the monitored pore pressure closed to the toe appears to be negative values, which is regarded as the contribution of soil dilation in related studies. As no dilation behavior is considered in the utilized model (dilation angle $\psi = 0^\circ$), the suction pressure is not well-captured in the numerical results. The use of more advanced constitutive model may alleviate the error and capture the negative pore-pressure value more accurately.

Figure 18 shows the final horizontal displacement profiles along the slope surface, which are in a good agreement with the experimental data.⁶² The movement direction of the slope toe is almost horizontal, whereas it changes to vertical motion at the slope crest. Therefore, larger horizontal displacement is observed at the vicinity of the toe. As the permeability decreases, the difference of the horizontal displacements between the lower part and the upper part of the slope is enlarged. This is caused by the larger pore-pressure value being generated at lower permeability, and hence, yielding to a softer response and forming a greater horizontal deformation. It should be noted, however, the permeability effect does not significantly change the general shape of the collapse (see Figure 19), which is mainly dominated by the soil's softening behavior.

6 | CONCLUSIONS

This paper presents a semi-implicit hydro-mechanical coupled MPM using a fractional-step method. The saturated porous medium with fully-incompressible pore-liquid flows is assumed in the formulation. The implicit treatment of the pore pressure of the water phase leads to a better stability in handling internal incompressibility constraint compared to the explicit counterpart. The method is also proven to reduce the numerical oscillations effectively yet with a significantly larger critical time step size. The proposed method eliminates the restriction on the critical time step from the compressibility of the liquid phase and the permeability of the soil. All the presented numerical tests are in good agreement with the analytical solutions for both 1D and 2D problems. Furthermore, the method is also demonstrated to be able to deal with an engineering-scale model, such as the slope-failure problem, with large deformation with realistic permeability condition.

Although the proposed method works efficiently and accurately for soil dynamics problems with large deformation, the time-step size is still subjected to a CFL condition to satisfy the strain increment level for the explicit stress integration. This correspondingly may hinder its application for specific problems, particularly, on static or quasi-static undrained problems, such as long-term consolidation cases or problems involving materials with very low permeability coefficient. In such long-term engineering problems, the pore-water pressure is dissipated in a very long time, and thus, larger time

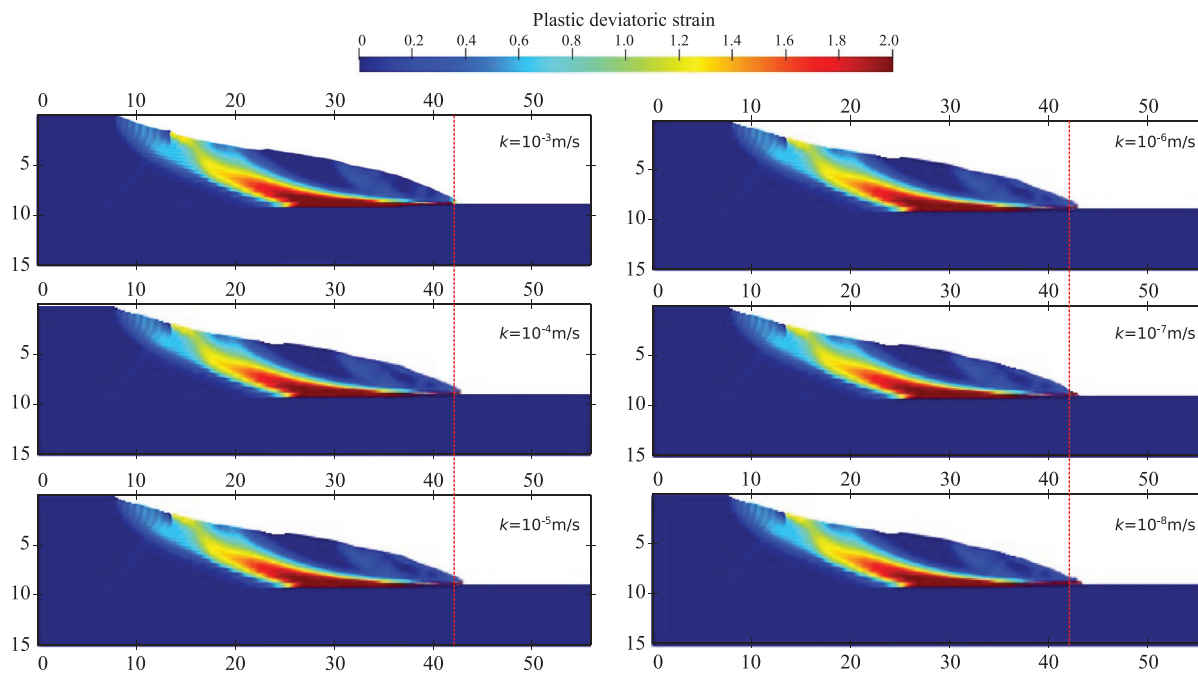


FIGURE 19 Final shape of the collapse with varying permeability k . The red dashed line indicates the reference position of the toe for case $k = 10^{-3}$ m/s. Color contour plots plastic deviatoric strain

step size will be required for modeling a period of several months or years. In this aspect, the fully implicit coupled mixed formulation,²⁶ which solves the displacement-pressure or velocity-pressure systems monolithically, seems to be a more appropriate option. Further research should focus on improving the efficiency of the matrix solver considering parallelism and investigation on the factors that influence the accuracy and stability of the method. Extension of the method to handle three-phase unsaturated soil is also an undergoing research topic.

ACKNOWLEDGMENTS

S. Kularathna, B. Chandra, and K. Soga gratefully acknowledge the support given by the Exxon Mobil Cooperation while conducting the research work. A grateful acknowledgement is also given to the overseas research grant provided by HKUST Research Grants Council of Hong Kong (GRF Project No. 16207319), and the China Scholarship Council (Grant No. 201806260197) for the valuable financial support during the research work conducted by W. Liang and T. Zhao in Berkeley, respectively. B. Chandra also specially thanks the support from the Jane Lewis Fellowship. The authors would like to thank Prof. K. Kumar from the University of Texas, Austin and Dr. E. Setiasabda for the fruitful discussions on the implementation aspect of the proposed formulation. [Correction added on May 21, 2021: Acknowledgment section has been updated to include funding by Research Grants Council of Hong Kong (GRF Project No. 16207319).]

AUTHOR CONTRIBUTION STATEMENT

Shyamini Kularathna: conceptualization, methodology, project administration, writing. **Weijian Liang** and **Tianchi Zhao** and **Bodhinanda Chandra:** methodology, software, validation, formal analysis, writing. **Jidong Zhao:** writing - reviewing and editing. **Kenichi Soga:** conceptualization, supervision, writing - review and editing.

DATA AVAILABILITY STATEMENT

Some or all data, models, or code that support the findings of this study are available from the corresponding author upon reasonable request.

ORCID

Weijian Liang  <https://orcid.org/0000-0001-8747-8952>

Bodhinanda Chandra  <https://orcid.org/0000-0003-2537-8213>

Jidong Zhao  <https://orcid.org/0000-0002-6344-638X>

REFERENCES

1. Ehlers W, Kubik J. On finite dynamic equations for fluid saturated porous media. *Acta Mech.* 1994;105:101-117.
2. Biot MA. General theory of three-dimensional consolidation. *J Appl Phys.* 1941;12(2):155-164.
3. Biot M. Theory of elasticity and consolidation for a porous anisotropic solid. *J Appl Phys.* 1955;26(2):182-185.
4. Biot M. Theory of propagation of elastic waves in a fluid saturated porous solid. I. Low-frequency range. *J Acoust Soc Am.* 1956;28(2):168-178.
5. Biot M. Mechanics of deformation and acoustic propagation in porous media. *J Appl Phys.* 1962;33(4):1482-1498.
6. Biot M. Theory of finite deformations of porous solids. *Indiana Univ Math J.* 1972;21(7):597-620.
7. Zienkiewicz O, Chan A, Pastor M, Schrefler B, Shiomi T. *Computational Geomechanics.* John Wiley and Sons Ltd.; 1999.
8. Zienkiewicz O, Shiomi T. Dynamic behaviour of saturated porous media: the generalized biot formulation and its numerical solution. *Int J Numer Anal Methods Geomech.* 1984;8:71-96.
9. Diebels S, Ehlers W. Dynamic analysis of a fully saturated porous medium accounting for geometrical and material non-linearities. *Int J Numer Methods Eng.* 1996;39:81-97.
10. Liew K, Ng T, Wu Y. Meshfree method for large deformation analysis—a reproducing kernel particle approach. *Eng Struct.* 2002;24(5):543-551.
11. Zhang H, Wang K, Chen Z. Material point method for dynamic analysis of saturated porous media under external contact/impact of solid bodies. *Comput Methods Appl Mech Eng.* 2009;198(17-20):1456-1472.
12. Zabala F, Alonso E. Progressive failure of Aznalcóllar Dam using the material point method. *Géotechnique.* 2011;61(9):795-808.
13. Jassim I, Stolle D, Vermeer P. Two-phase dynamic analysis by material point method. *Int J Numer Anal Methods Geomech.* 2013;37(15):2502-2522.
14. Yerro A, Alonso E, Pinyol N. The material point method for unsaturated soils. *Géotechnique.* 2015;65(3):201-217.
15. Bandara S, Ferrari A, Laloui L. Modelling landslides in unsaturated slopes subjected to rainfall infiltration using material point method. *Int J Numer Anal Methods Geomech.* 2016;40:1358-1380.
16. Zhang H, Wang K, Zhang Z. Material point method for numerical simulation of failure phenomena in multiphase porous media. In: *Computational Mechanics, ISCM2007.* Beijing, China: Tsinghua University Press and Springer; 2007:36-47.
17. Mackenzie-Helnwein P, Arduino P, Shin W, Moore JA, Miller GR. Modeling strategies for multiphase drag interactions using the material point method. *Int J Numer Methods Eng.* 2010;83:295-322.
18. Abe K, Soga K, Bandara S. Material point method for coupled hydromechanical problems. *J Geotech Geoenviron Eng.* 2014;140(3):04013033.
19. Bandara S, Soga K. Coupling of soil deformation and pore fluid flow using material point method. *Comput Geotech.* 2015;63:199-214.
20. Liu C, Sun Q, Jin F, Zhou GG. A fully coupled hydro-mechanical material point method for saturated dense granular materials. *Powder Technol.* 2017;314:110-120.
21. Sulsky D, Chen Z, Schreyer HL. A particle method for history-dependent materials. *Comput Methods Appl Mech Eng.* 1994;118(1):179-196.
22. Sulsky D, Zhou SJ, Schreyer HL. Application of a particle-in-cell method to solid mechanics. *Comput Phys Commun.* 1995;87(1-2):236-252.
23. Bardenhagen SG, Kober EM. The generalized interpolation material point method. *Comput Model Eng Sci.* 2004;5(6):477-496.
24. Soga K, Alonso E, Yerro A, Kumar K, Bandara S. Trends in large-deformation analysis of landslide mass movements with particular emphasis on the material point method. *Géotechnique.* 2016;66(3):248-273.
25. Babuska I, Narasimhan R. The Babuska-Brezzi condition and the patch test: an example. *Comput Methods Appl Mech Eng.* 1997;140(1-2):183-199.
26. Zhao Y, Choo J. Stabilized material point methods for coupled large deformation and fluid flow in porous materials. *Comput Methods Appl Mech Eng.* 2020;362:112742.
27. Malkus DS, Hughes TJ. Mixed finite element methods—reduced and selective integration techniques: a unification of concepts. *Comput Methods Appl Mech Eng.* 1978;15(1):63-81.
28. Hughes T. *The Finite Element Method - Linear Static and Dynamic Finite Element Analysis.* Englewood Cliffs, NJ: Prentice-Hall International, Inc.; 1987.
29. Chorin A. Numerical solution of the Navier-Stokes equations. *Math Comput.* 1968;22(104):745-762.
30. Gresho P, Sani R. *Incompressible Flow and the Finite Element Method.* Wiley; 1998.
31. Stomakhin A, Schroeder C, Jiang C, Chai L, Teran J, Selle A. Augmented MPM for phase-change and varied materials. *ACM Trans Graph.* 2014;33:1-11.
32. Kularathna S, Soga K. Implicit formulation of material point method for analysis of incompressible materials. *Comput Methods Appl Mech Eng.* 2017;313:673-686.
33. Zhang F, Zhang X, Sze KY, Lian Y, Liu Y. Incompressible material point method for free surface flow. *J Comput Phys.* 2017;330:92-110.
34. Kumar K, Salmond J, Kularathna S, et al. Scalable and modular material point method for large scale simulations. 2nd International Conference on the Material Point Method. Cambridge, UK. <https://arxiv.org/abs/1909.13380>. 2019.
35. Terzaghi K, Peck RB, Mesri G. *Soil Mechanics in Engineering Practice.* John Wiley & Sons; 1996.
36. Ceccato F, Yerro A, Martinelli M. Modelling soil-water interaction with the material point method. Evaluation of Single-Point and Double-Point Formulations. *Numerical Methods in Geotechnical Engineering IX.* Volume 1: Proceedings of the 9th European Conference on Numerical Methods in Geotechnical Engineering (NUMGE 2018) CRC Press; 2018:351.
37. Zienkiewicz OC, Chan AHC, Pastor M, Paul DK, Shiomi T. Static and dynamic behaviour of soils: a rational approach to quantitative solutions. I. Fully saturated problems. *Proc. R. Soc. Lond. A.* 1990;429(1877):285-309.

38. Markert B, Heider Y, Ehlers W. Comparison of monolithic and splitting solution schemes for dynamic porous media problems. *Int J Numer Methods Eng*. 2010;82(11):1341-1383.
39. Wang K, Sun W. A semi-implicit discrete-continuum coupling method for porous media based on the effective stress principle at finite strain. *Comput Methods Appl Mech Eng*. 2016;304:546-583.
40. Li X, Han X, Pastor M. An iterative stabilized fractional step algorithm for finite element analysis in saturated soil dynamics. *Comput Methods Appl Mech Eng*. 2003;192(35):3845-3859.
41. Kularathna S, Soga K. Comparison of two projection methods for modeling incompressible flows in MPM. *J Hydrodyn B*. 2017;29(3):405-412.
42. Bardenhagen S. Energy conservation error in the material point method for solid mechanics. *J Comput Phys*. 2002;180(1):383-403.
43. Fern EJ, Soga K. The role of constitutive models in MPM simulations of granular column collapses. *Acta Geotech*. 2016;11(3):659-678.
44. Carrier WD. Goodbye, Hazen; Hello, Kozeny-Carman. *J Geotech Geoenviron Eng*. 2003;129(11):1054-1056.
45. Liang W, Zhao J. Multiscale modeling of large deformation in geomechanics. *Int J Numer Anal Methods Geomech*. 2019;43(5):1080-1114.
46. Harlow FH. The particle-in-cell computing method for fluid dynamics. *Methods Comput Phys*. 1964;3:319-343.
47. Hamad FM. *Formulation of a Dynamic Material Point Method and Applications to Soil-Water-Geotextile Systems*. PhD thesis; 2014.
48. Marrone S, Colagrossi A, Le Touzé D, Graziani G. Fast free-surface detection and level-set function definition in SPH solvers. *J Comput Phys*. 2010;229(10):3652-3663.
49. Rosales RR, Seibold B, Shirokoff D, Zhou D. High-order finite element methods for a pressure Poisson equation reformulation of the Navier-Stokes equations with electric boundary conditions. *Comput Methods Appl Mech Eng*. 2021;373:113451.
50. Courant R, Friedrichs K, Lewy H. Über die partiellen Differenzgleichungen der mathematischen Physik. *Math Ann*. 1928;100(1):32-74.
51. Mieremet M, Stolle D, Ceccato F, Vuik C. Numerical stability for modelling of dynamic two-phase interaction. *Int J Numer Anal Methods Geomech*. 2016;40(9):1284-1294.
52. Huang M, Wu S, Zienkiewicz OC. Incompressible or nearly incompressible soil dynamic behaviour—a new staggered algorithm to circumvent restrictions of mixed formulation. *Soil Dyn Earthq Eng*. 2001;21(2):169-179.
53. Huang M, Yue ZQ, Tham LG, Zienkiewicz OC. On the stable finite element procedures for dynamic problems of saturated porous media. *Int J Numer Methods Eng*. 2004;61(9):1421-1450.
54. Prohl A. *Projection and Quasi-Compressibility Methods for Solving the Incompressible Navier-Stokes Equations*. Springer; 1997.
55. Terzaghi K. *Theoretical Soil Mechanics*. London: Chapman and Hall, Limited; 1951.
56. Steffen M, Kirby RM, Berzins M. Analysis and reduction of quadrature errors in the material point method (MPM). *Int J Numer Methods Eng*. 2008;76(6):922-948.
57. Nairn JA. Numerical simulation of orthogonal cutting using the material point method. *Eng Fract Mech*. 2015;149:262-275.
58. Jiang C, Schroeder C, Teran J. An angular momentum conserving affine-particle-in-cell method. *J Comput Phys*. 2017;338:137-164.
59. Mandel J. Consolidation Des Sols (Étude Mathématique). *Geotechnique*. 1953;3(7):287-299.
60. Gibson R, Schiffman R, Pu S. Plane strain and axially symmetric consolidation of a clay layer on a smooth impervious base. *Q J Mech Appl Math*. 1970;23(4):505-520.
61. Cooper M. The Progressive Development of a Failure Slip Surface in Over-Consolidated Clays at Selborne, UK. *Proceedings of the 7th International Symposium on Landslides, Trondheim*. Rotterdam: Balkema; 1996:683-688.
62. Cooper M, Bromhead E, Petley D, Grants D. The Selborne cutting stability experiment. *Géotechnique*. 1998;48(1):83-101.
63. Bandara SS. *Material Point Method to Simulate Large Deformation Problems in Fluid-Saturated Granular Medium*. PhD thesis. University of Cambridge Cambridge, UK; 2013.
64. Bromhead E, Cooper M, Petley D. The Selborne Cutting Slope Stability Experiment (CD-ROM). *The Selborne Data Collection CD*; 1998.
65. Robert DJ. *Soil-Pipeline Interaction in Unsaturated Soils*. PhD thesis. University of Cambridge; 2010.

How to cite this article: Kularathna S, Liang W, Zhao T, Chandra B, Zhao J, Soga K. A semi-implicit material point method based on fractional-step method for saturated soil. *Int J Numer Anal Methods Geomech*. 2021;45:1405–1436. <https://doi.org/10.1002/nag.3207>

APPENDIX A: EXPLICIT MPM ALGORITHM

This section presents the algorithm for standard explicit one-point two-phase MPM (Algorithm 2).

Algorithm 2 Explicit one-point two-phase MPM algorithm

- 1 **if** $t = 0$ **then**
- 2 # Initialize material points ;
- 3 volume: V_p^0 , density: $\rho_{\alpha,p}^0$, volume fraction: $n_{\alpha,p}^0$, particle mass: $m_{\alpha,p}^0 = n_{\alpha,p}^0 \rho_{\alpha,p}^0 V_p^0$;
- 4 particle initial total stress: σ_p^0 , pore pressure, p_p^0 , particle velocities: $\mathbf{v}_{s,p}^0$ and $\mathbf{v}_{f,p}^0$;
- 5 **while** $0 < t$ and $t \leq t_{end}$ **do**
- 6 Map particle mass and momentum to computational nodes, and compute nodal velocities – (48), (49) ;
- 7 Compute solid strain and effective stress – (50)-(53) ;
- 8 Compute fluid volumetric strain and pore pressure:

$$\Delta \varepsilon_{vol,p}^f = \text{tr} \left(\frac{1}{2} \Delta t \sum_{l=1}^{n_n} \left(\nabla N_I(\mathbf{x}_{p,centroid}^t) \hat{\mathbf{v}}_f^t + \left(\nabla N_I(\mathbf{x}_{p,centroid}^t) \hat{\mathbf{v}}_f^t \right)^T \right) \right),$$

$$p_p^{t+1} = p_p^t - \frac{K_f}{n_{f,p}} (n_{s,p} \Delta \varepsilon_{vol,p}^s + n_{f,p} \Delta \varepsilon_{vol,p}^f) ;$$
- 9 Update particle volume, density, volume fraction, and permeability – (55)-(58) ;
- 10 Compute nodal internal, external, and drag forces for fluid phase and the mixture:

$$\mathbf{f}_f^{int} = - \sum_{p=1}^{n_p} \nabla N_I(\mathbf{x}_p^t) (-n_{f,p} p_p^{t+1}) V_p^{t+1},$$

$$\mathbf{f}_f^{ext} = \sum_{p=1}^{n_p} \bar{\rho}_{f,p} N_I(\mathbf{x}_p^t) \mathbf{b} V_p^{t+1} + \int_{\partial \Omega} N_I(\mathbf{x}_p^t) \mathbf{t}_f dS,$$

$$\mathbf{f}_d = \sum_{p=1}^{n_p} \sum_{J=1}^{n_I} \frac{n_f^2 g \rho_f}{k} N_I(\mathbf{x}_p^t) N_J(\mathbf{x}_p^t) V_p^{t+1} (\hat{\mathbf{v}}_f - \hat{\mathbf{v}}_s),$$

$$\mathbf{f}_s^{int} = - \sum_{p=1}^{n_p} \nabla N_I(\mathbf{x}_p^t) : (\sigma_p^{t+1} - p_p^{t+1}) V_p^{t+1},$$

$$\mathbf{f}_s^{ext} = \sum_{p=1}^{n_p} \rho_p N_I(\mathbf{x}_p^t) \mathbf{b} V_p^{t+1} + \int_{\partial \Omega} N_I(\mathbf{x}_p^t) \mathbf{t} dS ;$$
- 11 Update nodal accelerations and velocities:

$$\hat{\mathbf{a}}_f^{t+1} = (\mathbf{f}_f^{int} + \mathbf{f}_f^{ext} - \mathbf{f}_d) / \hat{m}_f,$$

$$\hat{\mathbf{a}}_s^{t+1} = (\mathbf{f}_s^{int} + \mathbf{f}_s^{ext} - \hat{\mathbf{a}}_f^{t+1} \hat{m}_f) / \hat{m}_s,$$

$$\hat{\mathbf{v}}_\alpha^{t+1} = \hat{\mathbf{v}}_\alpha^t + \Delta t \hat{\mathbf{a}}_\alpha^{t+1} ;$$
- 12 Update particle velocity and acceleration – (72)-(74) ;
- 13 $t = t + \Delta t$
- 14 Note: In step 8 of this algorithm, the volumetric strain for the fluid phase is evaluated at the centroid of the cell to enhance the stability of computation, following Bandara and Soga¹⁹.